NASA Technical Memorandum 88286

Thermal Stress Analysis of Space Shuttle Orbiter Subjected to Reentry Aerodynamic Heating

William L. Ko and Roger A. Fields
Ames Research Center, Dryden Flight Research Facility, Edwards, California

1987

National Aeronautics and
Space Administration
Ames Research Center
Dryden Flight Research Facility
Edwards, California 93523-5000

SUMMARY

A structural performance and resizing (SPAR) finite-element computer program and NASA structural analysis (NASTRAN) finite-element computer programs were used in the thermal stress analysis of the space shuttle orbiter subjected to reentry aerodynamic heating. A SPAR structural model was set up for the entire left wing of the orbiter, and NASTRAN structural models were set up for (1) a wing segment located at midspan of the orbiter left wing and (2) a fuselage segment located at midfuselage. The thermal stress distributions in the orbiter structure were obtained and the critical high thermal stress regions were identified. It was found that the thermal stresses induced in the orbiter structure during reentry were relatively low. The thermal stress predictions from the whole wing model were considered to be more accurate than those from the wing segment model because the former accounts for temperature and stress effects throughout the entire wing.

INTRODUCTION

The space shuttle orbiter is designed to be flown as many as 100 missions without excess thermal and mechanical loadings. To establish confidence in the orbiter thermal and structural integrity, it is essential to fully understand both the thermal and structural performance of the orbiter subjected to reentry aerodynamic heating and aerodynamic loading.

Because the number of onboard thermocouples is extremely limited, it is impossible to generate accurate temperature distribution within the orbiter structure based on thermocouple data for estimation of the temperature in each structural component. For this reason analytical thermal analysis (for example, finite-element heat transfer analysis) of the orbiter is necessary. The thermal analysis can give relatively accurate temperature distribution in the orbiter structure, making it possible to determine the temperature level in each of the orbiter structural components. This analysis can show if the design limit temperature of 350°F is exceeded. (Heating beyond 350°F will certainly degrade the aluminum structural material.) Additionally, a thorough knowledge of the structural temperature distribution is necessary for an accurate thermal stress analysis.

The flight load data obtained from onboard strain gage measurements contain both the thermal and mechanical stresses. Unfortunately, these two stress components are not easily separated experimentally. To obtain the mechanical stresses, the thermal stresses must be removed from the strain-gage-measured stresses. This can be done analytically by first calculating the thermal stresses and then removing them from the strain-gage-measured stresses to give the true mechanical stresses. For the thermal stress calculations, the structural temperature distributions obtained from the heat transfer analysis may be used as input to a structural model. Extensive work on the heat transfer analysis of the orbiter was conducted by Ko, Quinn, and Gong (refs. 1 to 7).

The purpose of this report is to use the finite-element method to calculate thermal stresses in the orbiter structure using the structural temperature distributions obtained from references 4 to 7 as thermal loadings to the structural models. Finite-element structural models were set up for the entire left wing, a wing segment

located at midspan of the left wing, and a fuselage segment located at midfuselage. Thermal stress distributions in the orbiter structure were obtained, and the critical high-stress regions were identified. These analyses also provide a baseline for establishing element mesh sizes which will be adequate for thermal stress analysis of large aerospace structures.

NOMENCLATURE

CQUAD2	quadrilateral membrane and bending element
CROD	two-node tension/compression/torsion element
E23	bar element
E25	zero-length element for elastically connected geometrically coincident joints
E31	triangular membrane element
E41	quadrilateral membrane element
E44	quadrilateral shear panel element
FRSI	flexible felt reusable surface insulation
FS877	fuselage segment structural model at station X_0877
HRSI	high-temperature reusable surface insulation
JLOC	joint location (or node)
LRSI	low-temperature reusable surface insulation
NASTRAN	NASA structural analysis
RTV	room temperature vulcanized
SIP	strain isolation pad
SPAR	structural performance and resizing
STS-5	space transportation system, flight 5
TPS	thermal protection system
WING	whole wing structural or thermal model
WS240	wing segment structural or thermal model at wing station $\lvert Y_0 \rvert$ 240
X_0	station in x direction

Y_0	station in y direction
Z_0	station in z direction
x, y, z	rectangular Cartesian coordinates
$\Delta\alpha$	change in angle of attack, deg
σ_x	normal stress in x direction, lb/in^2
σ_y	normal stress in y direction, lb/in^2
τ_{xy}	shear stress, lb/in^2

DESCRIPTION OF PROBLEM

Figure 1 shows a composite top and bottom view of the space shuttle orbiter. The orbiter parts selected for the present study are the major load-carrying regions of the left wing, and the midfuselage cross section (fig. 1). The problem is to calculate thermal stresses induced in the space shuttle orbiter structure during reentry aerodynamic heating. The thermal loadings to the orbiter structure were based on the space transportation system flight 5 (STS-5) reentry trajectory shown in figure 2 (ref. 4). Three regions of the orbiter were selected for the thermal stress analysis. The first region was the whole left wing bounded by chordwise stations $X_0$1040 and $X_0$1365. The second region was a segment of the left wing bounded by spanwise stations Y_0-240 and Y_0-254. The third region was a fuselage segment bounded by fuselage stations $X_0$877 and $X_0$880. The elevon, leading edge regions, wheel well door, and bay door were not included in the analysis because the present study concerns only the major load-carrying structures. Also the thermal protection system (TPS) was excluded in the thermal stress analysis because it is not a load-carrying structural component. However, for the heat transfer analysis, the wheel well door, the landing gear, the bay door, and the TPS had to be included.

DESCRIPTION OF STRUCTURES

Wing

As shown in figure 3, the ribs of the wing are aluminum truss systems made of vertical, horizontal, and diagonal members pin-joined together. All of the spar webs, the wheel well vertical walls, and the wing root vertical wall (fuselage wall) are made of corrugated aluminum panels. Both the lower and upper wing skins lying between stations $X_0$1191 and $X_0$1365 are made of hat-stringer-reinforced aluminum panels. The lower and upper wing skins lying between stations $X_0$1040 and $X_0$1191, and the leading edge beam assembly are made of aluminum honeycomb-core sandwich panels. The landing gear door is made of double-walled, hat-stringer-reinforced aluminum panels separated by aluminum stringers. The entire lower wing surface is covered with high-temperature reusable surface insulation (HRSI) tiles, with a

layer of strain isolation pad (SIP) lying between the wing skin and the HRSI for the absorption of strain incompatibility between the aluminum wing skin and the HRSI. Most of the upper skin near the leading edge region is covered with low-temperature reusable surface insulation (LRSI) tiles. A SIP layer lies under the LRSI to function the same as the SIP does for the HRSI. The rest of the upper wing skin, which is subjected to low heating, is covered with highly flexible felt reusable surface insulation (FRSI), under which there is no SIP layer. Room temperature vulcanized (RTV) rubber bonding agent was used in bonding the thermal protection system (TPS) to the wing surfaces. Some of the gaps between the TPS tiles in the high-temperature regions are filled with ceramic-coated aluminum mat (gap fillers) to prevent hot gases from coming in contact with the substructure at the bottom of each gap. Figure 4 shows the structural details of the wing segment of the orbiter right wing.

Fuselage

Figure 5 shows the fuselage cross section located at station X_0877. Both the fuselage bottom (or belly) and the sidewall are made of T-stiffener-reinforced aluminum skins. The lower and the upper glove skins (except for the leading edge region) are made of hat-stringer-reinforced aluminum skins. The leading edge region of the glove skin is an aluminum honeycomb-core sandwich structure. The bay door is a sandwich structure made of honeycomb core and graphite-epoxy composite skins. A small portion of the bay door inner surface is covered with a layer of RTV rubber to serve as a heat sink. The fuselage bottom, lower glove, glove leading edge region, and part of the glove upper surface (near the leading edge region) are covered with HRSI. Most of the upper glove outer surface is covered with LRSI. The lower portion of the sidewall outer surface is covered with FRSI, and the upper portion with LRSI. The upper outer surface of the payload bay door is covered with a layer of FRSI, and lower outer surface with LRSI.

FINITE-ELEMENT MODELING

Because of the complex nature of the space shuttle orbiter structure, some structural simplifications were necessary before setting up the finite-element structural models so that the computations would be manageable. Excessively detailed models could lead to excess computation time, for which the gain in solution accuracies might not be high enough compared with the solutions obtained from simpler yet reasonably detailed models. The previous heat transfer analysis of the orbiter (refs. 1 to 7) showed that representing the hat-stringer-reinforced skins (wing and glove skins), T-stiffener-reinforced fuselage skin, and honeycomb-core sandwich skins with smooth panels of effective thicknesses could give sufficiently accurate temperature solutions. Therefore, in setting up the structural models for the orbiter, a similar approach was adopted.

For the thermal stress analysis of the whole orbiter left wing, a structural performance and resizing (SPAR) finite-element computer program (ref. 8) was used; for the thermal stress analysis of the wing and fuselage segments, a NASA structural analysis (NASTRAN) computer program (ref. 9) was used.

Whole Wing

The SPAR finite-element structural model (WING) setup for the entire orbiter left wing is shown in figure 6. This wing structural model was obtained from direct modification of the whole wing thermal model used earlier for the heat transfer analysis by Ko, Gong, and Quinn (ref. 4). The wing upper and lower skins were modeled with quadrilateral membrane (E41) and triangular membrane (E31) elements. Only two elements were modeled between spar caps, and only one element between the rib caps. The anisotropic material properties were used to account for the effect of the hat-stringers. The fuselage wall (or wing root wall) was modeled with E41 elements. The spar and rib webs and the loading edge beam assembly were modeled with quadrilateral shear panel (E44) elements. The spar and rib caps and the rib truss members were modeled with two-mode bar elements (E23) which have only axial stiffness. The wing root nodes are elastically connected to geometrically coincident points through zero-length E25 elements to simulate the connection of the wing root to the fuselage structure. The size of the entire wing structural model is as follows:

232	JLOCs
498	E23 elements
10	E25 elements
181	E41 elements
19	E31 elements
67	E44 elements

Wing Segment

The NASTRAN finite-element structural model (WS240) for the orbiter wing segment bounded by wing stations Y_O-240 and Y_O-254, is shown in figure 7. The upper and lower wing skins, spar webs, and rib cap webs were modeled with quadrilateral membrane and bending elements (CQUAD2). The spar caps and the rib truss members were modeled with two-node tension-compression-torsion elements (CROD).

In order to approximate the actual deformation field of the whole wing, two boundary conditions were used for the WS240 structural model. The Y_O-254 plane was fixed (no displacement in the y direction), but the displacements in the x and z directions were permitted. For the Y_O-240 plane, two boundary conditions were used:

1. Plane stress — No rotations with respect to the x, y, and z axes, but free to move in the x, y, and z directions.

2. Plane strain deformation — The y displacements for all the nodes lying in the Y_O-240 plane were set identically, and rotations with respect to the x, y, and z axes were constrained.

The size of the entire WS240 structural model is as follows:

204	grid points
121	CQUAD2 elements
139	CROD elements

Fuselage Segment

Figure 8 shows the NASTRAN finite-element structural model (FS877) setup for the fuselage segment, bounded by the two planes at fuselage stations X_0877 and X_0880. The bay door was omitted because it is not a major load-carrying structure. The fuselage segment was modeled with CQUAD2 and CROD elements. The X_0877 plane was fixed (no displacement in the x direction), but the displacements in the y and z directions were permitted. The deformation of the X_0880 plane was constrained to be plane strain deformation. The entire FS877 structural model has

62	grid points
89	CQUAD2 elements
9	CROD elements

THERMAL LOADINGS

Figure 9 (taken from ref. 4) and figure 10 (taken from ref. 5) respectively show the structural temperature time histories for the wing skins and the fuselage skin. Notice that the structural temperatures for most of the wing skin and fuselage skin stations reached their respective peak values at t = 1700 sec from start of reentry. In this analysis, the structural temperature distributions at t = 1700 sec were used as thermal load input to the structural models for the thermal stress calculations.

For both WS240 and WING structural models, the structural temperature distributions were obtained from the computer outputs of the earlier heat transfer analysis conducted by Ko, Quinn, and Gong (ref. 4). For the FS877 model, the structural temperature distribution was obtained from the computer outputs of the heat transfer analysis done by Ko, Quinn, and Gong (ref. 5). Figure 11 shows the thermal loadings at wing station $|Y_0|$ 240 for the WS240 and WING structural models. The difference in the shape of the calculated structural temperature distributions in figure 11 is caused by the number of elements in the two models. Similar distribution can be expected in the thermal stress calculations. Figure 12 shows the thermal loading used for the FS877 structural model.

RESULTS

Figures 13 to 15 respectively show the distributions of the chordwise stress σ_x, spanwise stress σ_y, and the shear stress τ_{xy} in the orbiter wing lower skin calculated from the WING structural model. The peak compression of both σ_x (= -9097 lb/in^2) and σ_y (= -2897 lb/in^2) occurred near the wing root. The peak tension of σ_x = 2836 lb/in^2 and σ_y = 2405 lb/in^2 occurred at the leading edge region (figs. 13 and 14). The orbiter wing skin buckling stresses are approximately σ_x = -12,000 lb/in^2 and σ_y = -25,000 lb/in^2. The peak value of the shear stress $|\tau_x|$ = 7877 lb/in^2 was located at the wing root trailing edge zone (fig. 15). Figures 16 to 18 respectively show the distributions of σ_x, σ_y, and τ_{xy} in the orbiter wing upper skin. The peak tension of σ_x = 3087 lb/in^2 occurred near the wheel well, and

the peak compression of σ_x = -2947 lb/in^2 was located at the wing root trailing edge region (fig. 16). For σ_y, the peak tension 2483 lb/in^2 was located at the midspan trailing edge region, and the peak compression (σ_y = -1371 in/lb^2) occurred at the first bay of midspan (fig. 17).

Like the orbiter wing lower skin, the maximum shear $|\tau_{xy}|$ = 2137 lb/in^2 was located at the wing root trailing edge region. Figure 19 shows the shear stress distribution in the wing spars, leading edge panels, wing root wall, and the elevon support panels. The peak shear occurred at the trailing edge region of the wing root wall (fuselage wall).

Figure 20 shows the axial stresses in the orbiter wing spar caps, wing root rib caps, and other rod elements. The maximum axial tension of 7988 lb/in^2 occurred in the aft wheel well wall lower spar cap; the peak axial compression of -15,408 lb/in^2 occurred at the wing root rib lower cap near the midchord region. Figure 21 gives the axial stresses in the orbiter wing rib truss members. The peak tension of 5412 lb/in^2 occurred at the vertical truss member of the last bay of the rib next to to the wing root rib; the peak compression of -9038 lb/in^2 occurred at the lower horizontal truss member of the wing root rib.

Figures 22 to 24 respectively show the chordwise distributions of three thermal stresses σ_x, σ_y, and τ_{xy} at wing cross section Y_0-240. These stresses were calculated using the WS240 and WING structural models. For the WS240 model, two sets of curves were presented. The first set (solid curves) is for the "plane stress" boundary condition and the second set (dotted curves) is for the "plane strain" deformation. In figure 23, the distribution of σ_y calculated from WS240 model for the wing lower skin and upper skin of bay 1 exhibits stress release zones near the center region of each bay. This implies that the wing skins in those regions have bulged out because of thermal loading. The WING model did not have the capability to show the above stress release effect because of insufficient finite elements. Poor correlation between the predictions based on WS240 and predictions based on WING models could be attributed to:

1. The two sets of boundary conditions used for the WS240 model may not represent the actual deformation conditions.

2. The elements used for the WING model could be too coarse to give more accurate stress distributions.

The variations between the calculated stress data of figures 22 to 24 illustrate how sensitive the wing segment models are to boundary conditions. More importantly, the differences between the calculated stresses from the wing segment model and the wing model are significant in terms of percentage and sign. Even though the wing model is relatively coarse, it is still considered to be the most accurate analysis (of those presented here) because it considers temperature and stress effects throughout the entire wing. The WING model is also believed to be the least susceptible to those boundary conditions imposed in the case of the wing segment model. An increased number of elements in the entire wing model should improve the distribution of calculated stresses between spar caps, but the magnitude and range of stresses would be expected to change very little.

Figure 25 shows the distribution of the axial stress σ_x in the fuselage structure. The peak compression of $\sigma_x = -7653$ lb/in^2 in the fuselage bottom skin occurred near the vertical wall, and the peak tension of $\sigma_x = 7385$ lb/in^2 occurred near the glove leading edge region. Tables 1 and 2 summarize the major peak stresses that occurred in the orbiter major structural components.

Figure 26 shows the deflection curves of the orbiter wing leading and trailing edges. The wingtip deflection induced by the thermal loading is 0.94 in. The inner span region of the wing is twisted in the direction of increasing angle of attack, but the outer span region of the wing is twisted in the opposite direction. Figure 27 shows the spanwise change in angle of attack $\Delta\alpha$ as a result of the thermal loading. The maximum value of $|\Delta\alpha| = 0.1°$ occurred near the wingtip.

Figure 28 shows the deformed shapes of the wing cross section at Y_0-240 predicted by using the wing segment model under the two boundary conditions mentioned earlier. The entire wing cross section has curved up slightly because of thermal loading. The deformation at bay 1 is most conspicuous for boundary condition 1 (fig. 28(a)), with a vertical displacement of 0.110 in. at the bay 1 lower skin (honeycomb-core sandwich skin). For boundary condition 2 (fig. 28(b)), the peak vertical displacement of 0.121 in. occurred at the bay 1 upper skin. Figure 29 shows the deformed fuselage cross section at $X_0$877. The thermal loading tended to flatten the fuselage outer bottom, and caused the glove leading edge to move slightly upward, with upward displacement of 0.013 in.

CONCLUSIONS

Thermal stress analyses were performed on the space shuttle orbiter subjected to STS-5 reentry thermal loading. The whole wing, one midspan wing segment, and one midfuselage segment were selected for the analyses. The whole wing was found to be twisted under the thermal loading. The inboard span region of the wing is twisted in the direction of increasing angle of attack, but the outer span region of the wing is twisted in the opposite direction. The maximum twist angle of the wing is about 0.12°. The correlation between the stress predictions using the whole wing model and the wing segment model was rather poor. The reasons for this may be (1) the boundary conditions used in the wing segment model may not accurately represent the actual deformation field in the whole wing and (2) the whole wing model could be too coarse to give sufficiently accurate stress distributions. Even though the wing model is relatively coarse, it is still considered to be the most accurate analysis compared with the wing segment model because it considers temperature and stress effects throughout the entire wing. The fuselage cross section was found to deform in such a way that the fuselage outer bottom was slightly flattened and the glove leading edge moved slightly upward. Finally, it was found that the thermal stress levels induced in the orbiter structure were relatively low.

REFERENCES

1. Ko, William L.; Quinn, Robert D.; Gong, Leslie; Schuster, Lawrence S.; and Gonzales, David: Preflight Reentry Heat Transfer Analysis of Space Shuttle. AIAA-81-2382, AIAA/SETP/SETE/SAE 1st Flight Testing Conf., Las Vegas, Nev., Nov. 11-13 1981.

2. Ko, William L.; Quinn, Robert, D.; Gong, Leslie; Schuster, Lawrence S.; and Gonzales, David: Reentry Heat Transfer Analysis of the Space Shuttle Orbiter. Computational Aspects of Heat Transfer in Structures, NASA CP-2216, 1982, pp. 295-325.

3. Gong, Leslie; Quinn, Robert, D.; and Ko, William L.: Reentry Heating Analysis of Space Shuttle With Comparison of Flight Data. Computational Aspects of Heat Transfer in Structures, NASA CP-2216, 1982, pp. 271-294.

4. Gong, Leslie; Ko, William L.; and Quinn, Robert D.: Thermal Response of Space Shuttle Wing During Reentry Heating. NASA TM-85907, 1984.

5. Ko, William L.; Quinn, Robert D.; and Gong, Leslie: Finite-Element Reentry Heat-Transfer Analysis of Space Shuttle Orbiter. NASA TP-2657, 1986.

6. Ko, William L.; Quinn, Robert D.; and Gong, Leslie: Effects of Forced and Free Convections on Structural Temperatures of Space Shuttle Orbiter During Reentry Flight. NASA TM-86800, 1986.

7. Gong, Leslie; Ko, William L.; and Quinn, Robert D.: Comparison of Flight-Measured and Calculated Temperatures on the Space Shuttle Orbiter. NASA TM-88278, 1986.

8. Whetstone, W.D.: SPAR Structural Analysis System Reference Manual, System Level 13A, vol. 1, Program Execution. NASA CR-158970-1, 1978.

9. The NASTRAN User's Manual. Level 17.5, NASA SP-222(05), 1978.

TABLE 1. – PEAK STRESSES IN ORBITER STRUCTURAL COMPONENTS

Structural component	σ_x, lb/in^2		σ_y, lb/in^2		$\lvert \tau_{xy} \rvert$, lb/in^2
	Peak tension	Peak compression	Peak tension	Peak compression	Peak shear
Wing lower skin (Fig. 13 to 15)	2836	-9097	2405	-2897	7877
Wing upper skin (fig. 16 to 18)	3087	-2947	2483	-1371	2137
SPAR web/fuselage wall (fig. 19)	----	-----	----	-----	1829
Fuselage skin (fig. 27)	7411	-7628	533	-574	69

TABLE 2. – PEAK AXIAL STRESSES IN ORBITER SLENDER STRUCTURAL COMPONENTS

Structural component	Axial tension, lb/in^2	Axial compression, lb/in^2
Wing spar caps and wing root rib caps (fig. 20)	7988	-15,408
Wing rib truss members (fig. 21)	5412	-9,038

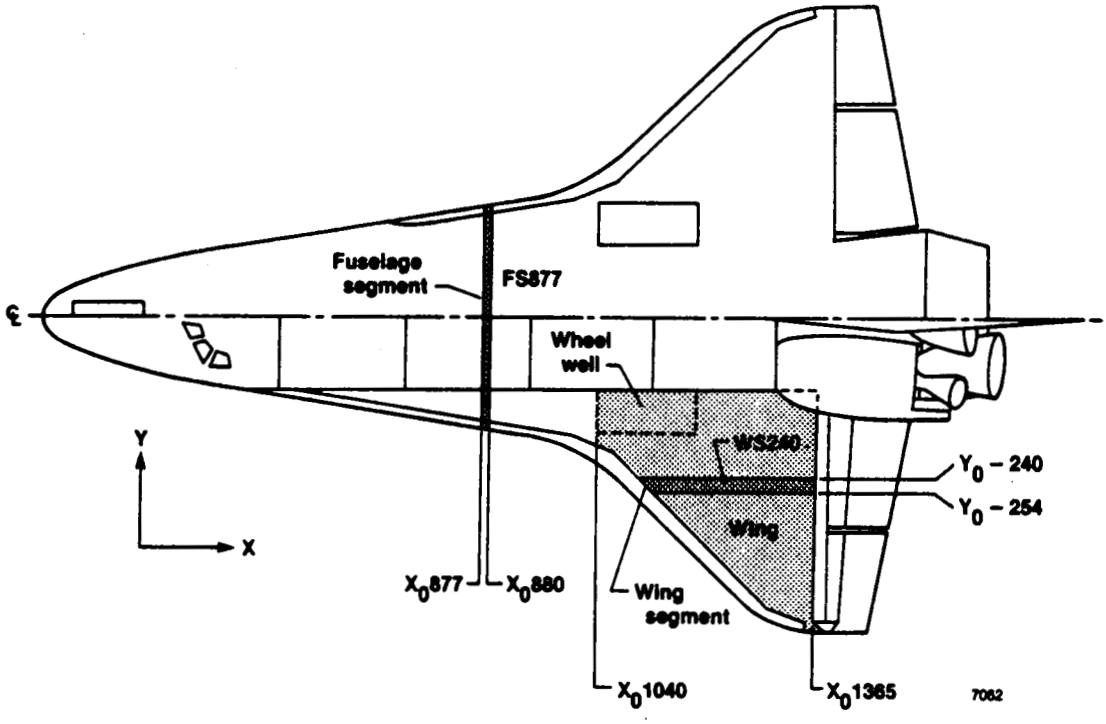

Figure 1. Regions of space shuttle orbiter modeled.

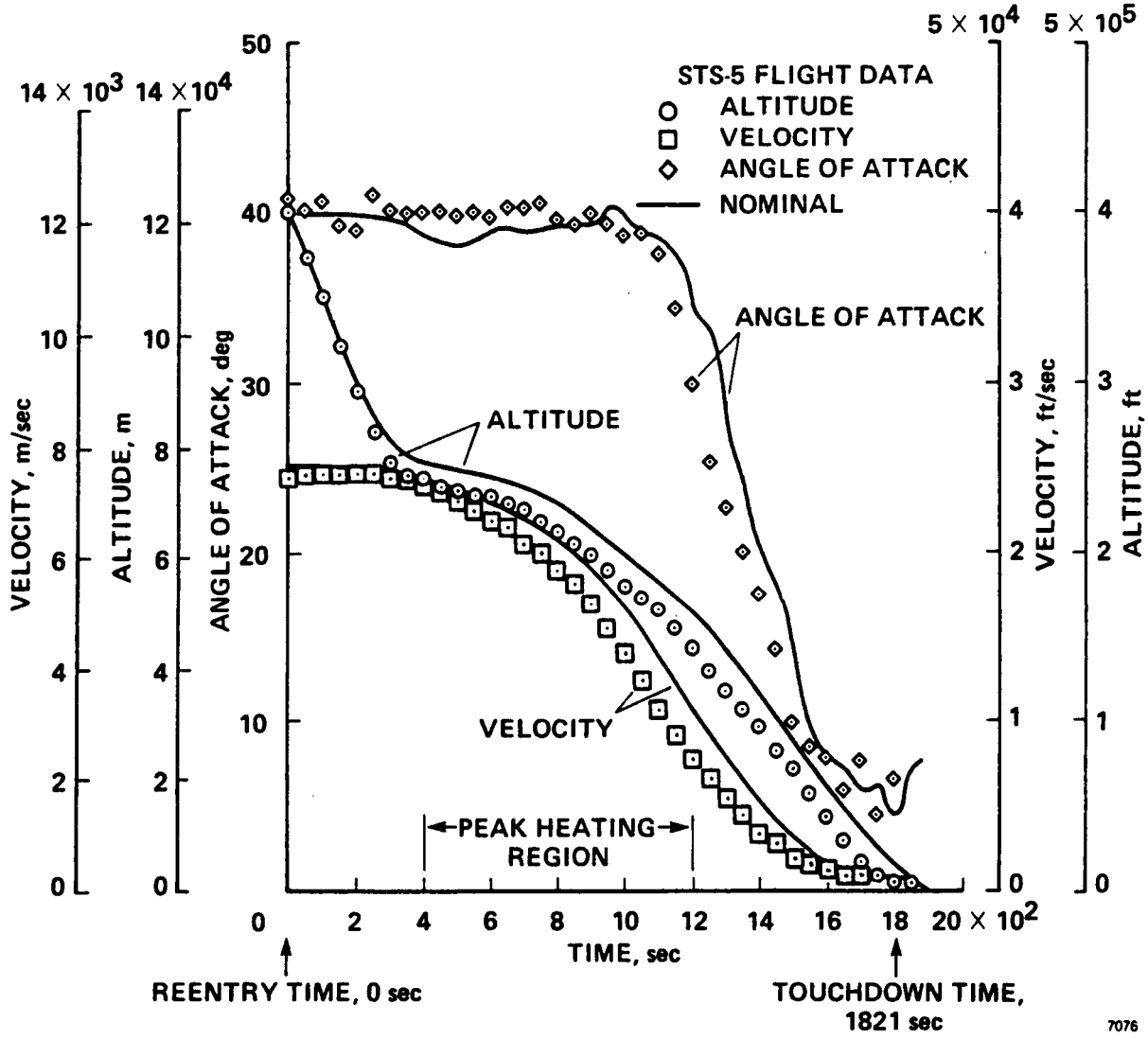

Figure 2. STS-5 trajectory (ref. 14).

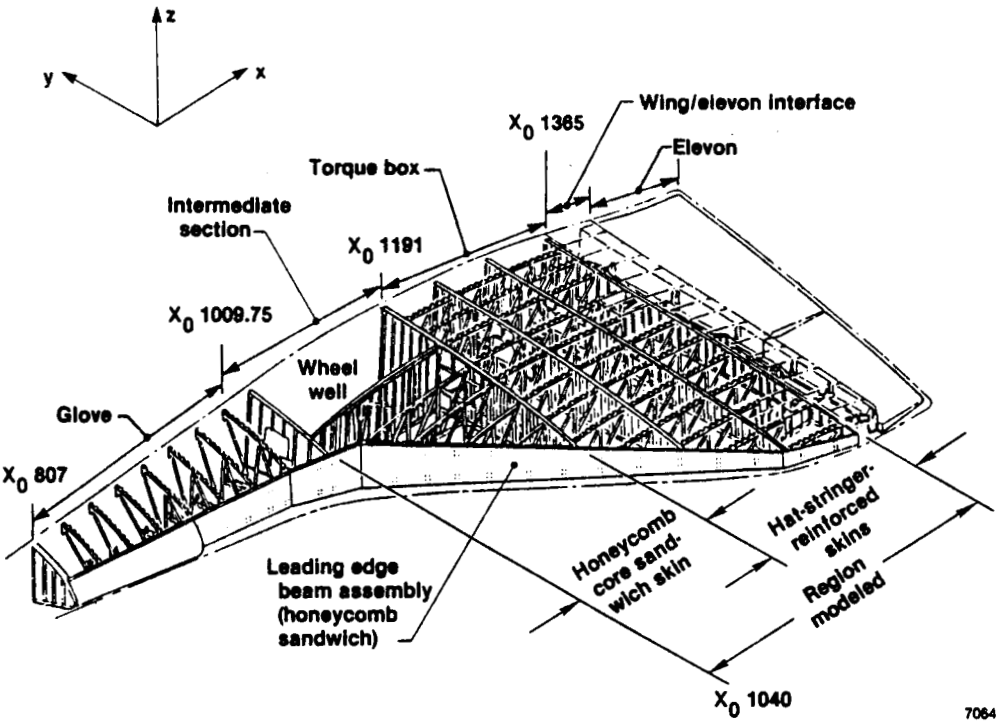

Figure 3. Space shuttle orbiter wing.

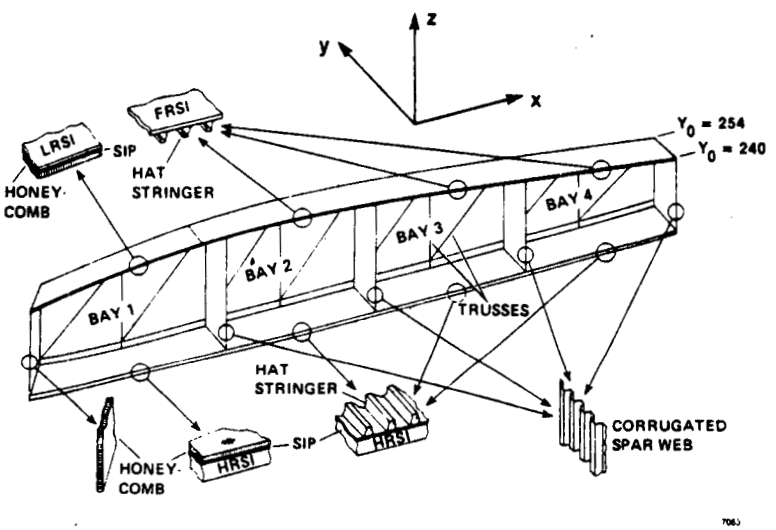

Figure 4. Geometry of wing segment WS240 between wing stations Y_0240 and Y_0254.

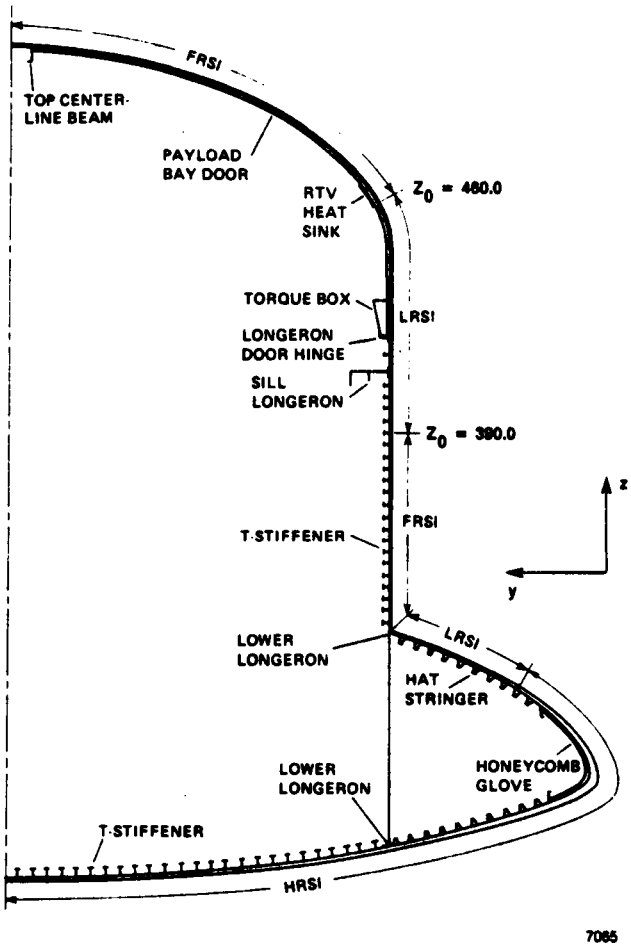

Figure 5. Geometry of fuselage cross section at X_0877.

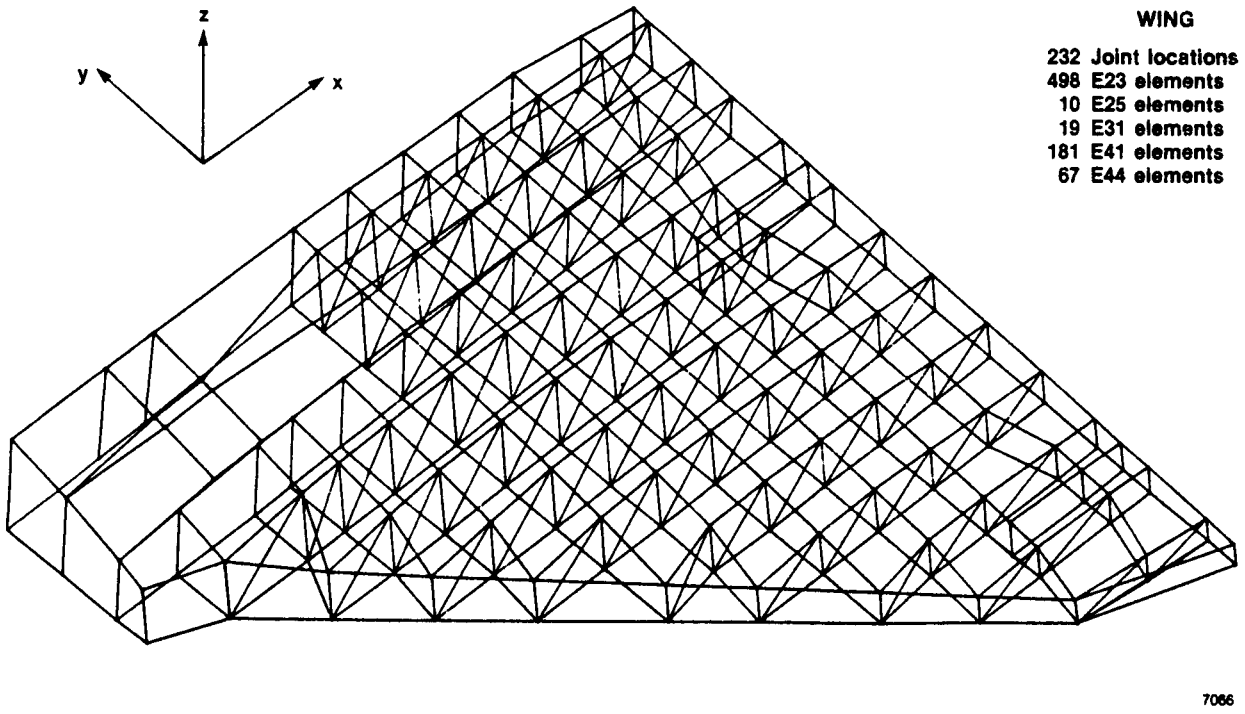

Figure 6. Space shuttle orbiter wing SPAR structural model. TPS, wheel well door, and landing gear excluded.

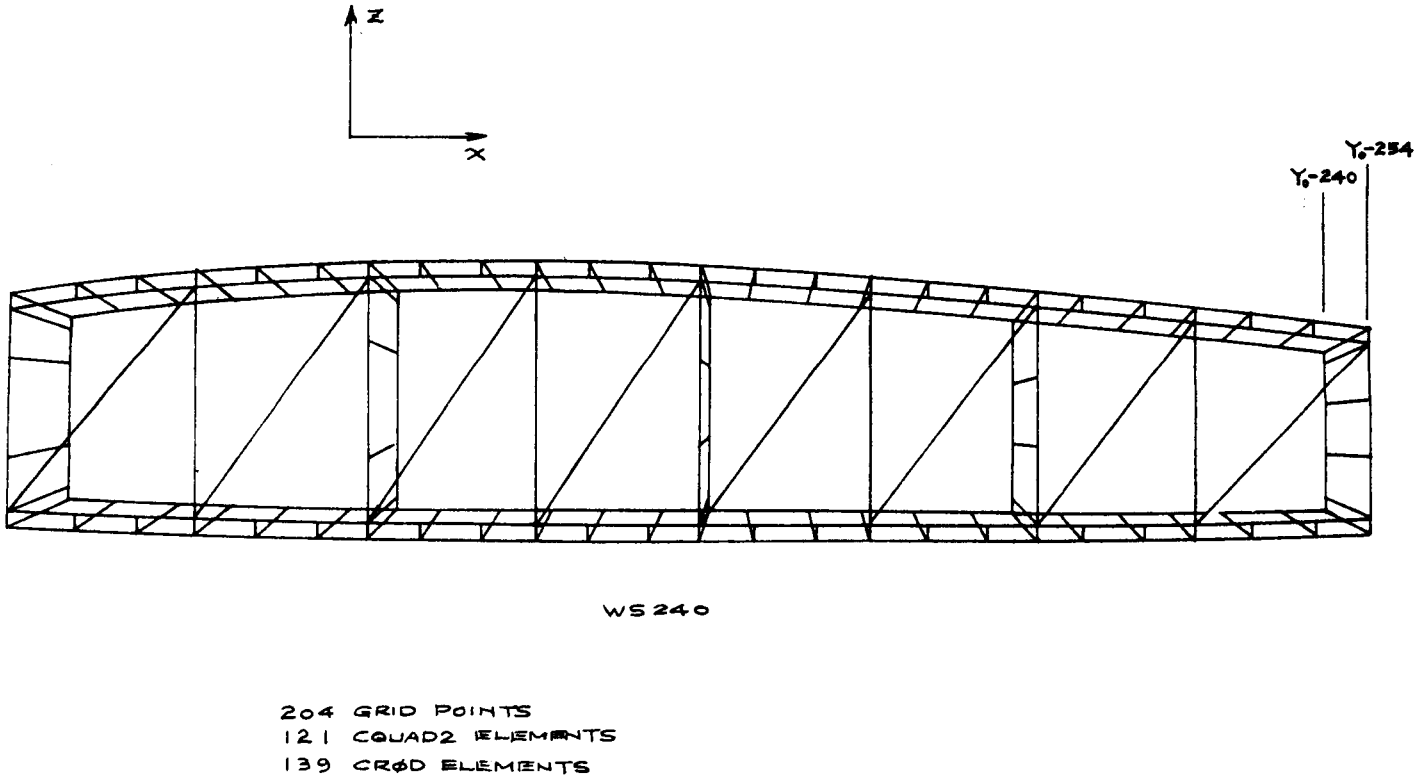

Figure 7. NASTRAN structural model for orbiter wing segment WS240.

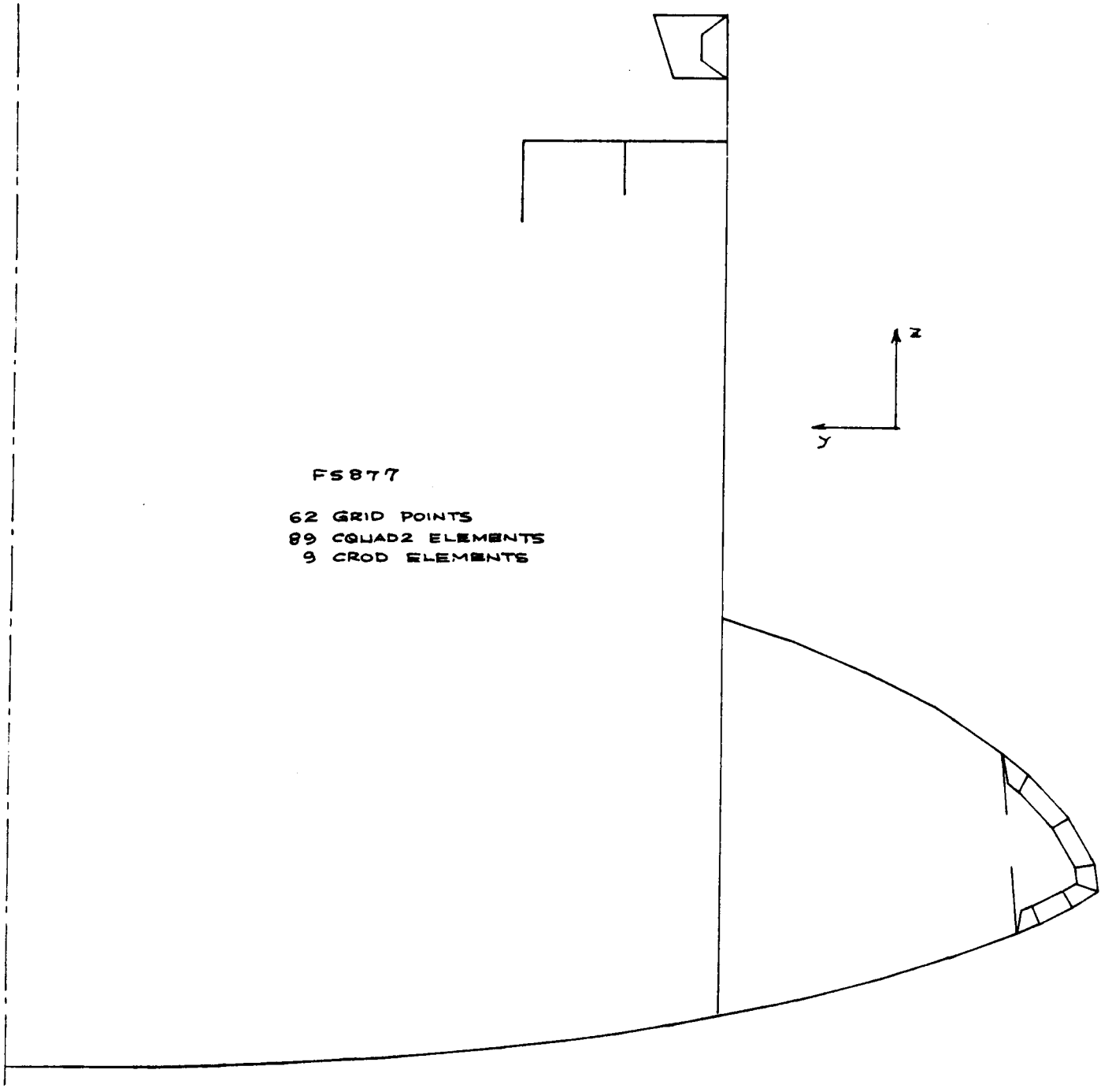

Figure 8. NASTRAN structural model for orbiter fuselage segment FS877.

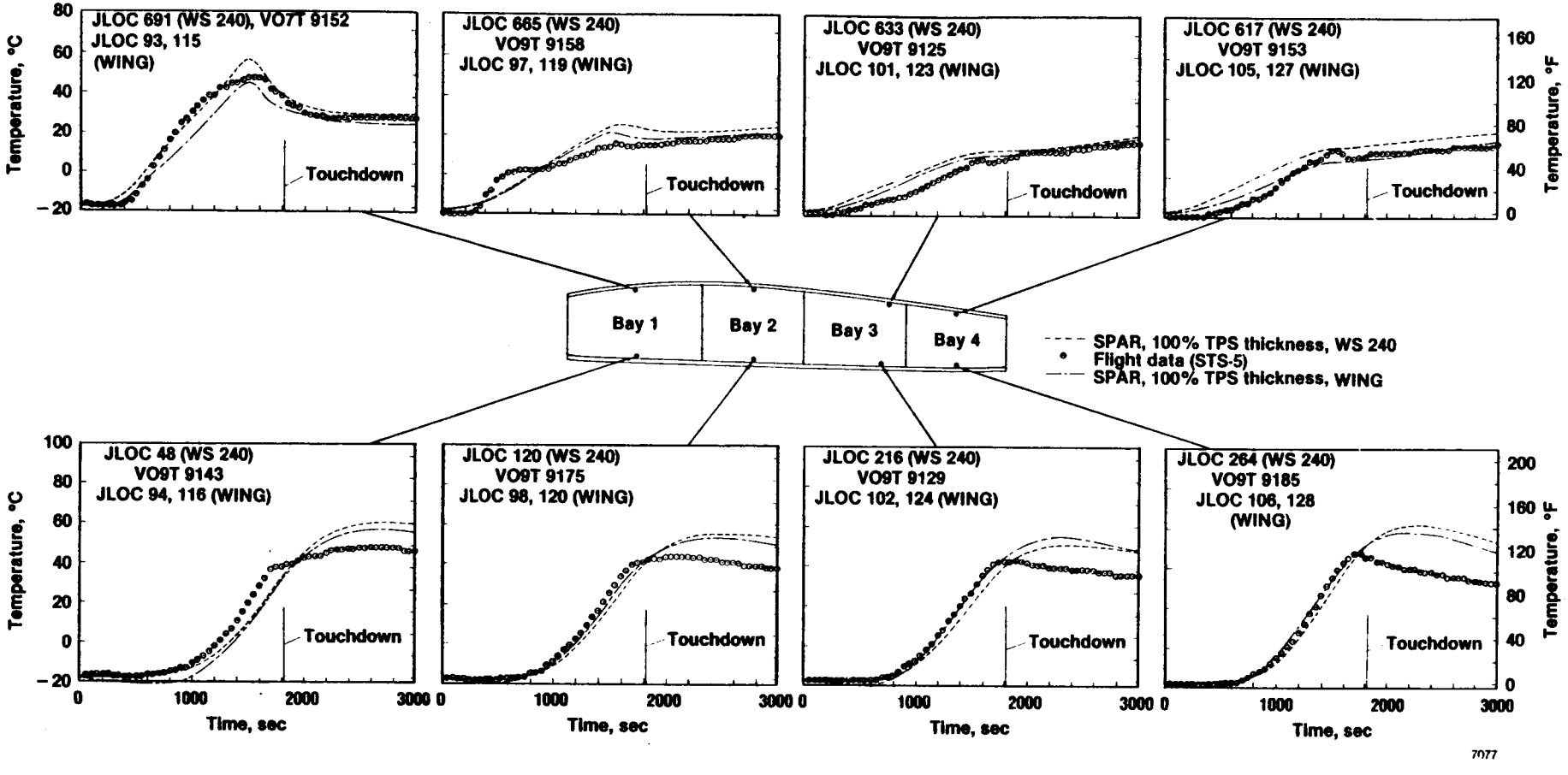

Figure 9. Orbiter wing skin temperature — time histories at station $|Y_O|$ 240. STS-5 flight (ref. 4).

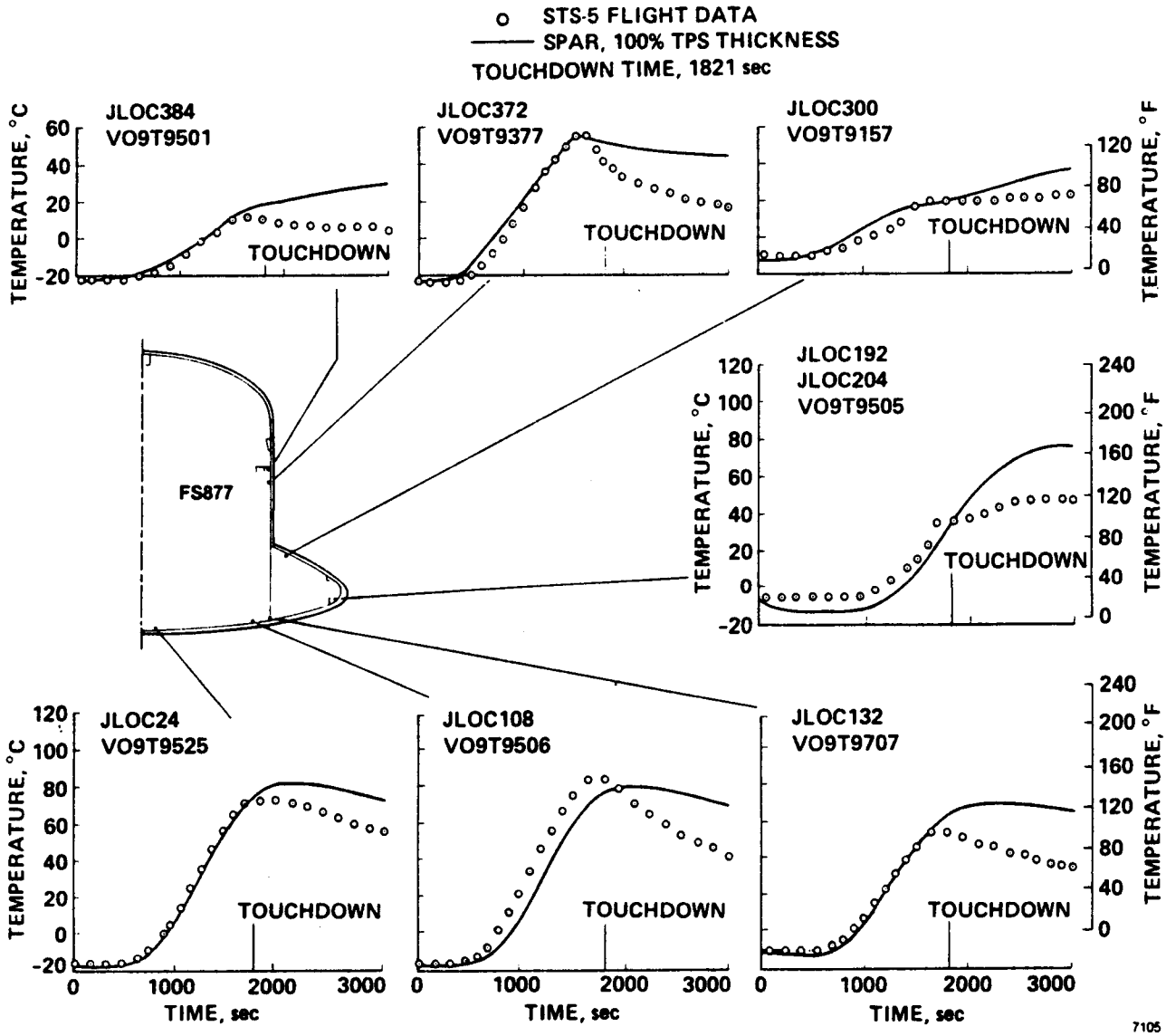

Figure 10. Orbiter fuselage skin temperature — time histories at station X_O877. STS-5 flight (ref. 5).

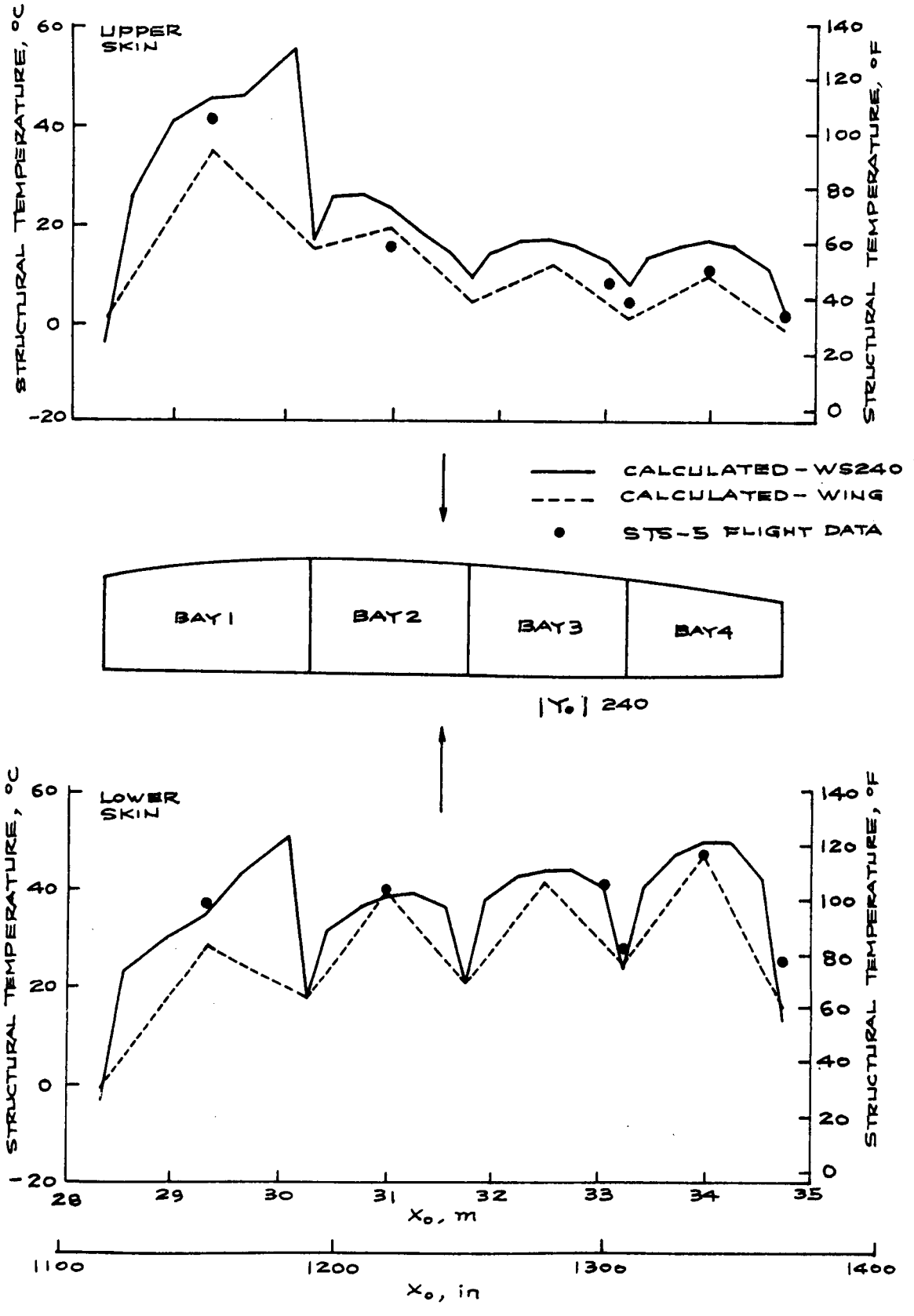

Figure 11. Chordwise distribution of aluminum skin temperatures at wing station $|Y_0|$ 240. Time = 1700 sec. STS-5 flight.

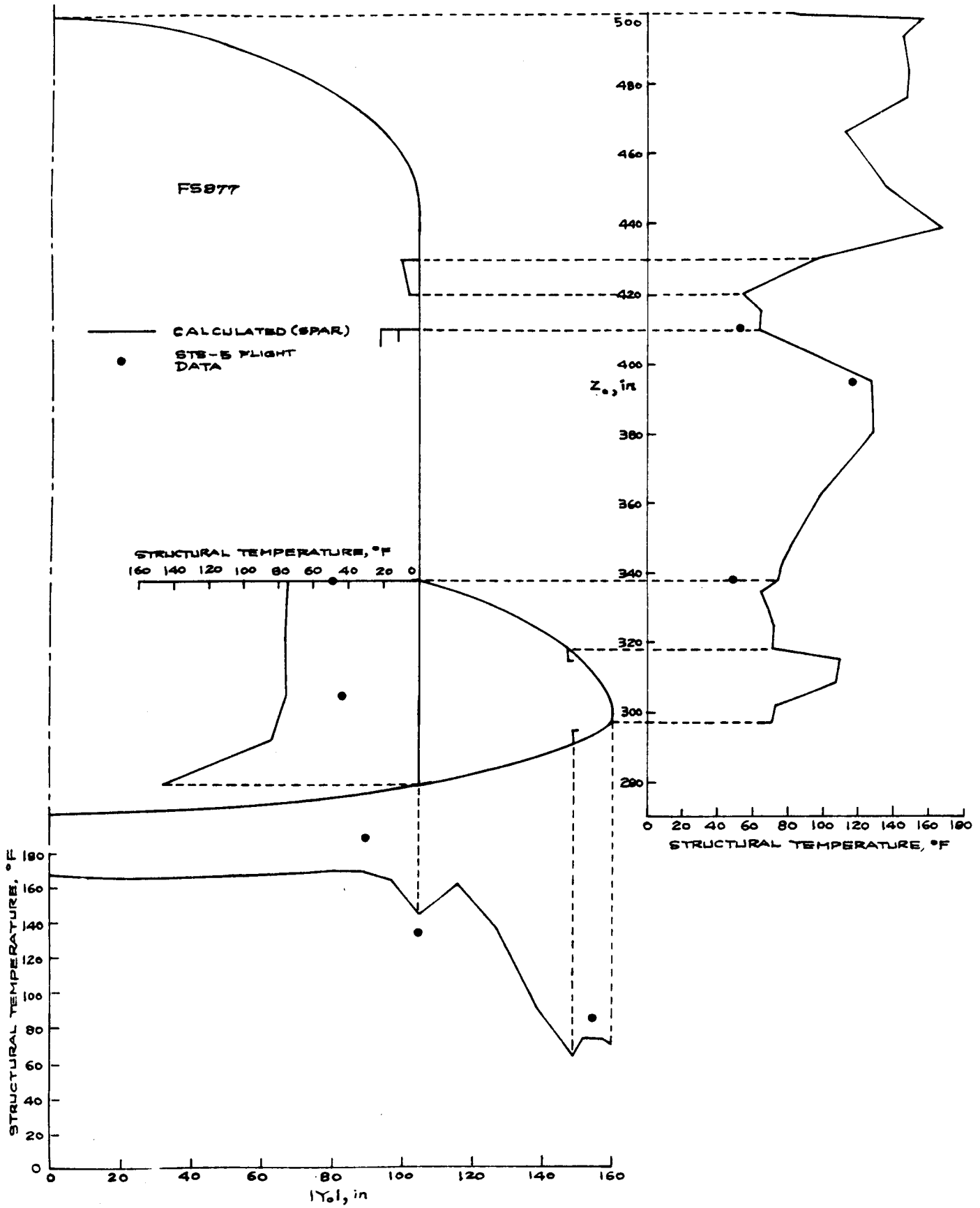

Figure 12. Circumferential distribution of fuselage structural temperature at station $X_0$877. STS-5 heating. Time = 1700 sec.

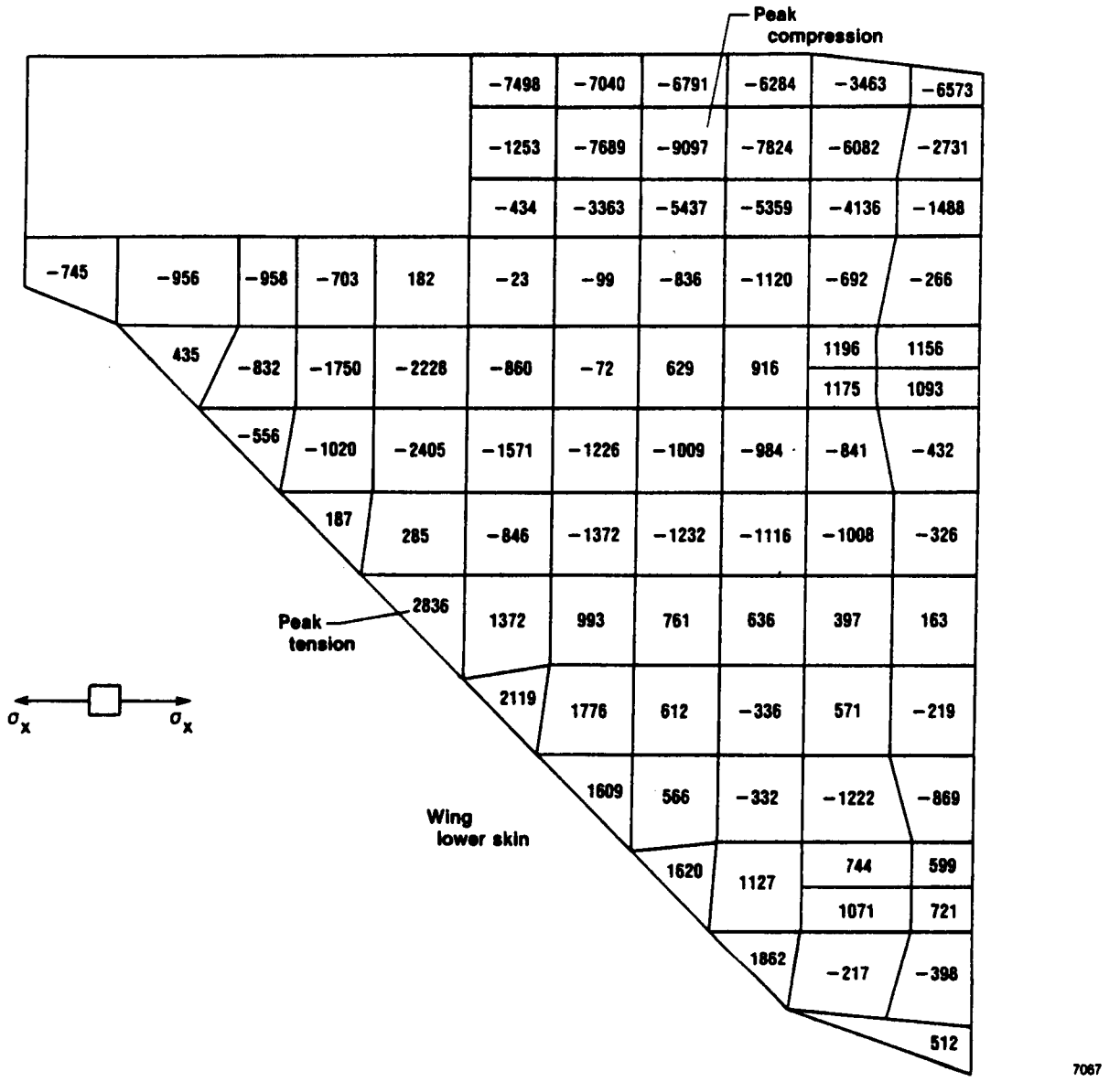

Figure 13. Distribution of normal stress σ_x (in lb/in^2) in the orbiter wing lower skin. STS-5 thermal loading. Time = 1700 sec.

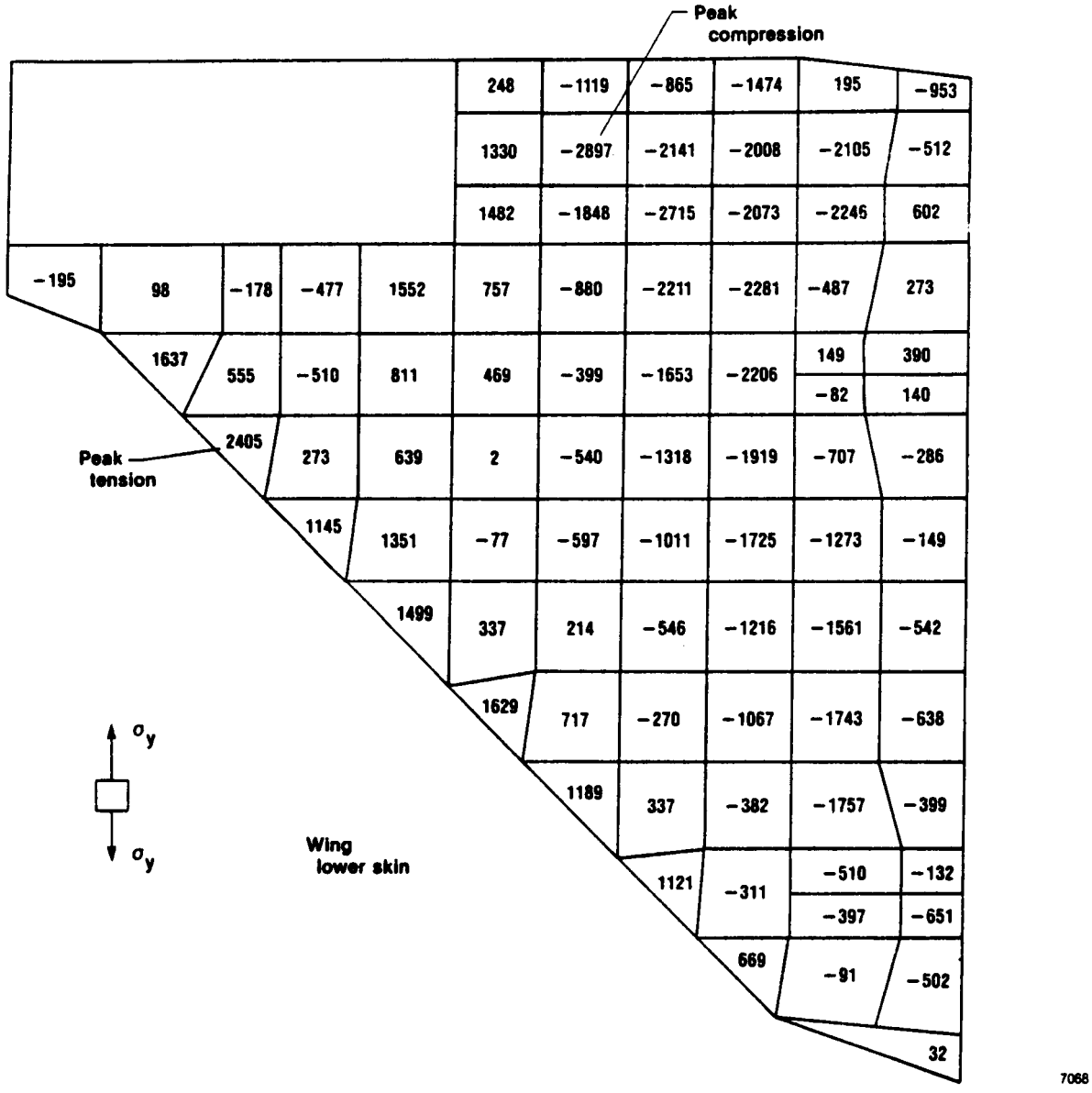

Figure 14. Distribution of normal stress σ_y (in lb/in^2) in the orbiter wing lower skin. STS-5 thermal loading. Time = 1700 sec.

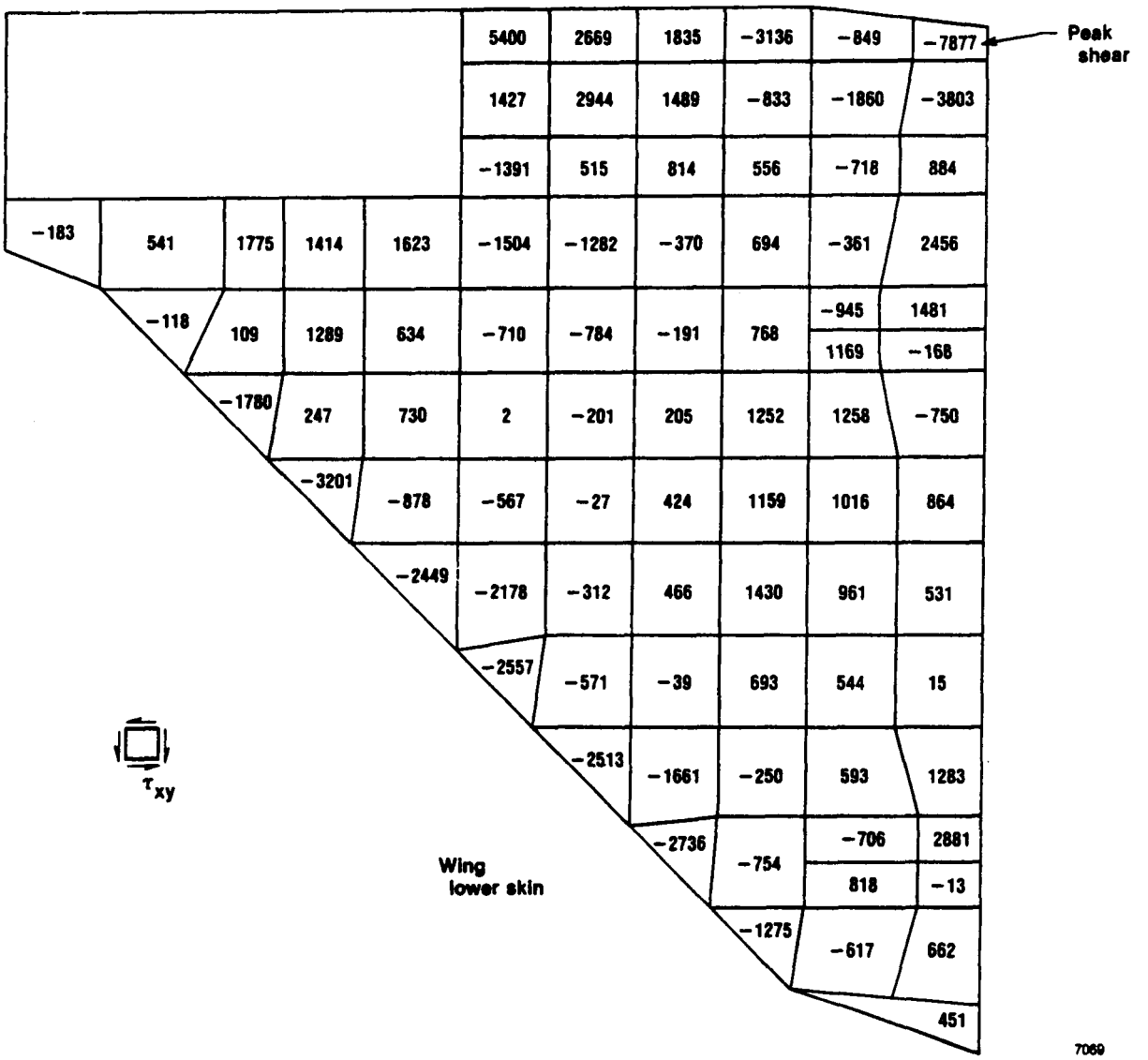

Figure 15. Distribution of shear stress τ_{xy} (in lb/in^2) in the orbiter wing lower skin. STS-5 thermal loading. Time = 1700 sec.

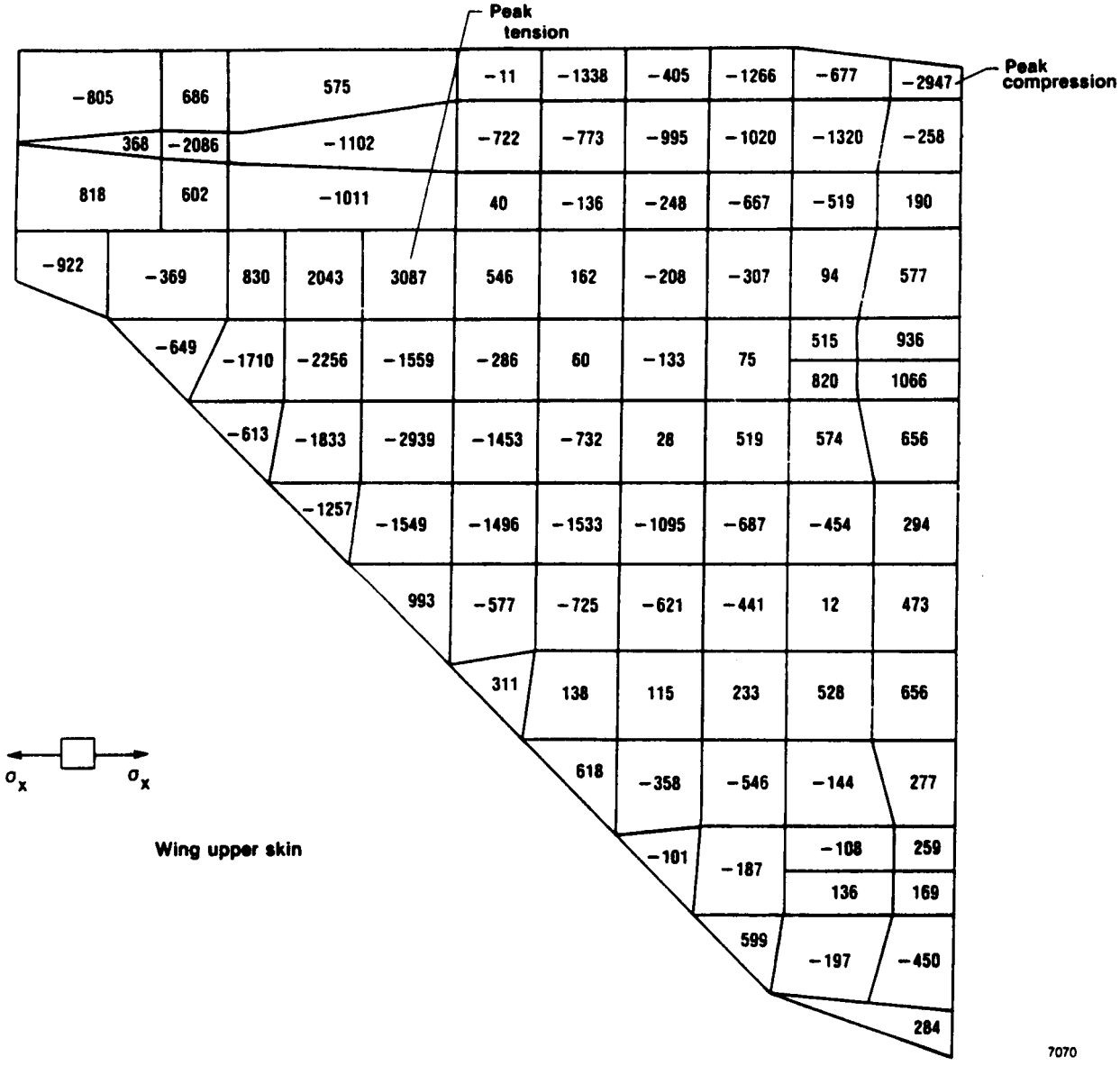

Figure 16. Distribution of normal stress σ_x (in lb/in^2) in the orbiter wing upper skin. STS-5 thermal loading. Time = 1700 sec.

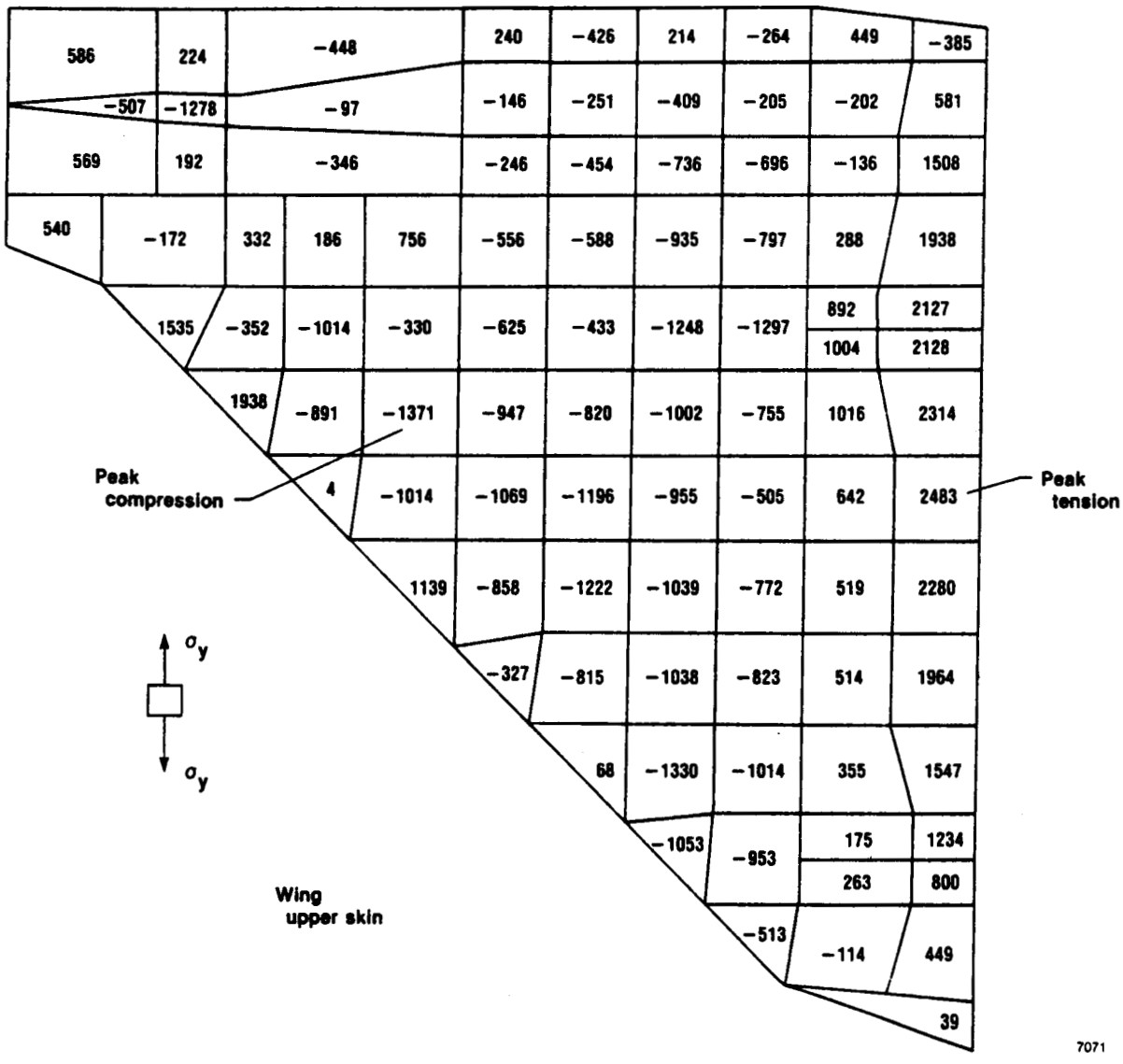

Figure 17. Distribution of normal stress σ_y (in lb/in^2) in the orbiter wing upper skin. STS-5 thermal loading. Time = 1700 sec.

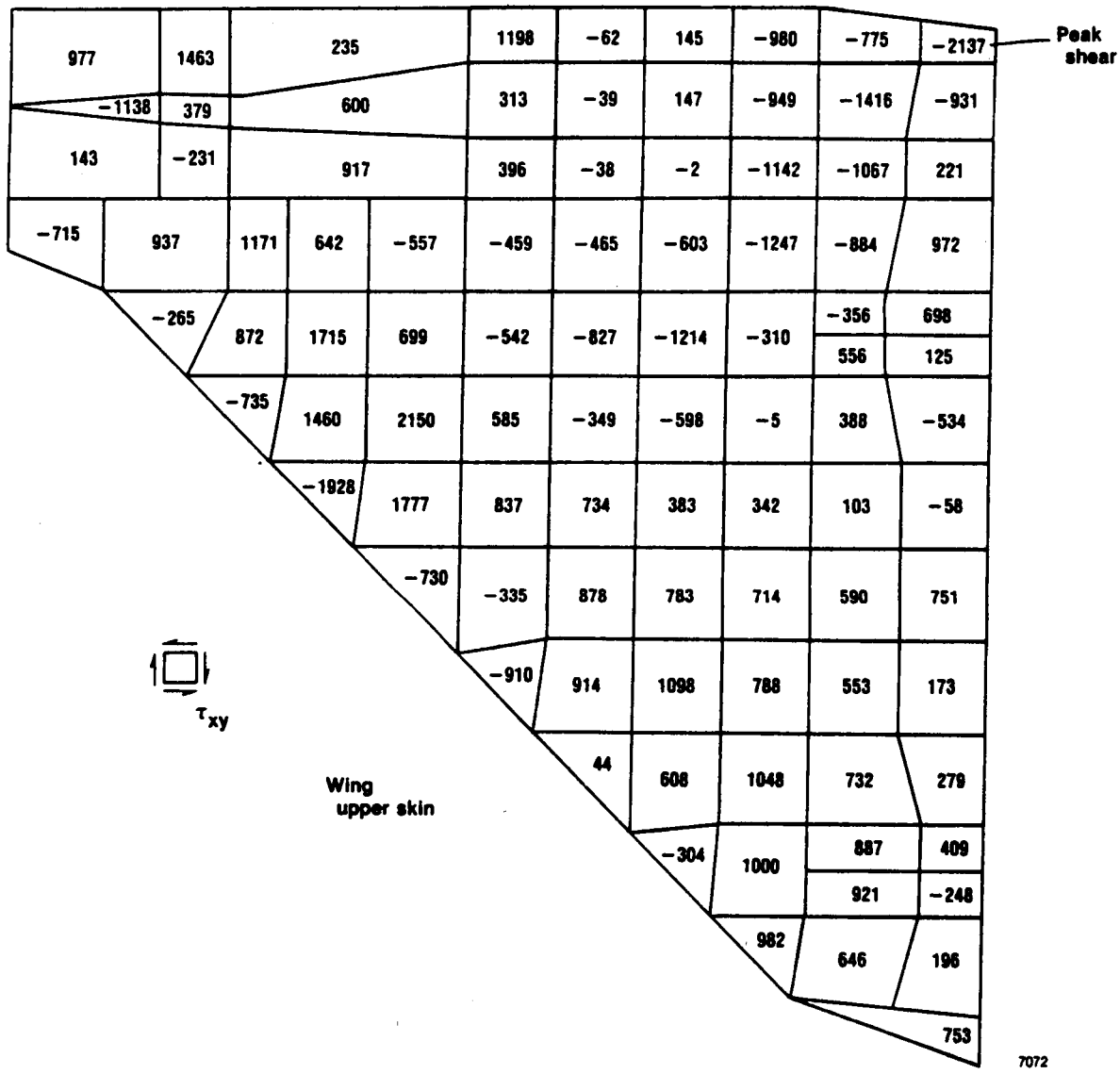

Figure 18. Distribution of shear stress τ_{xy} (in lb/in^2) in the orbiter wing upper skin. STS-5 thermal loading. Time = 1700 sec.

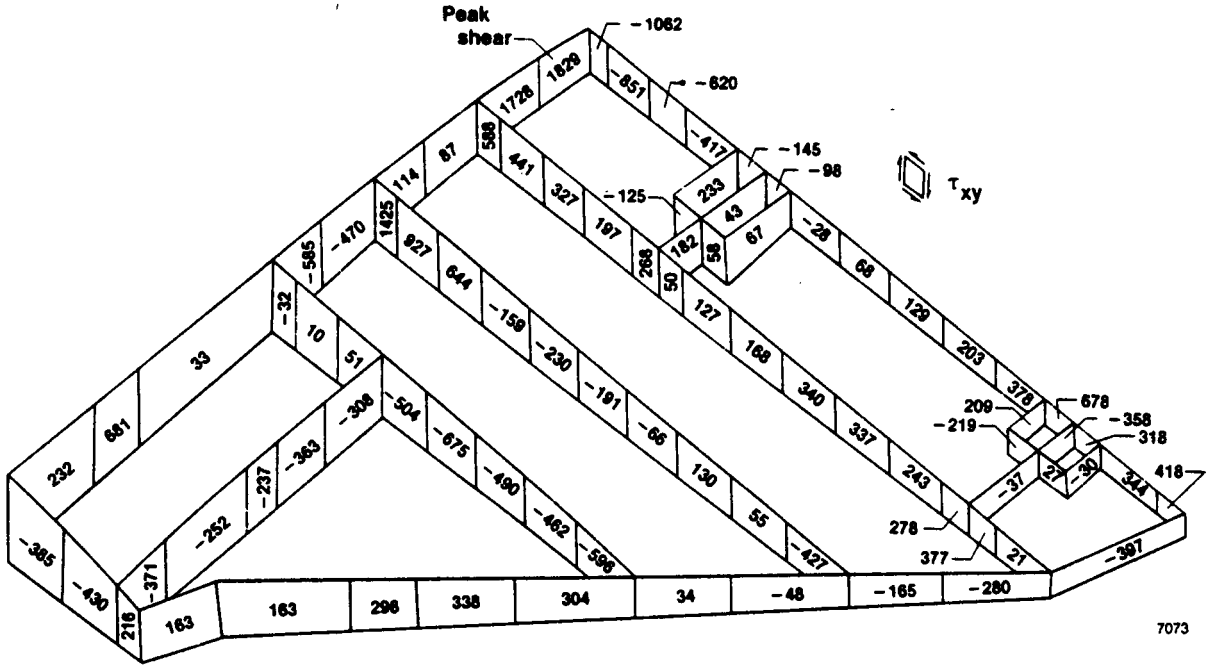

Figure 19. Distribution of shear stress τ_{xy} (in lb/in^2) in the orbiter wing spars, leading edge panel, wheel well walls, elevon support panels, and wing root wall. STS-5 thermal loading. Time = 1700 sec.

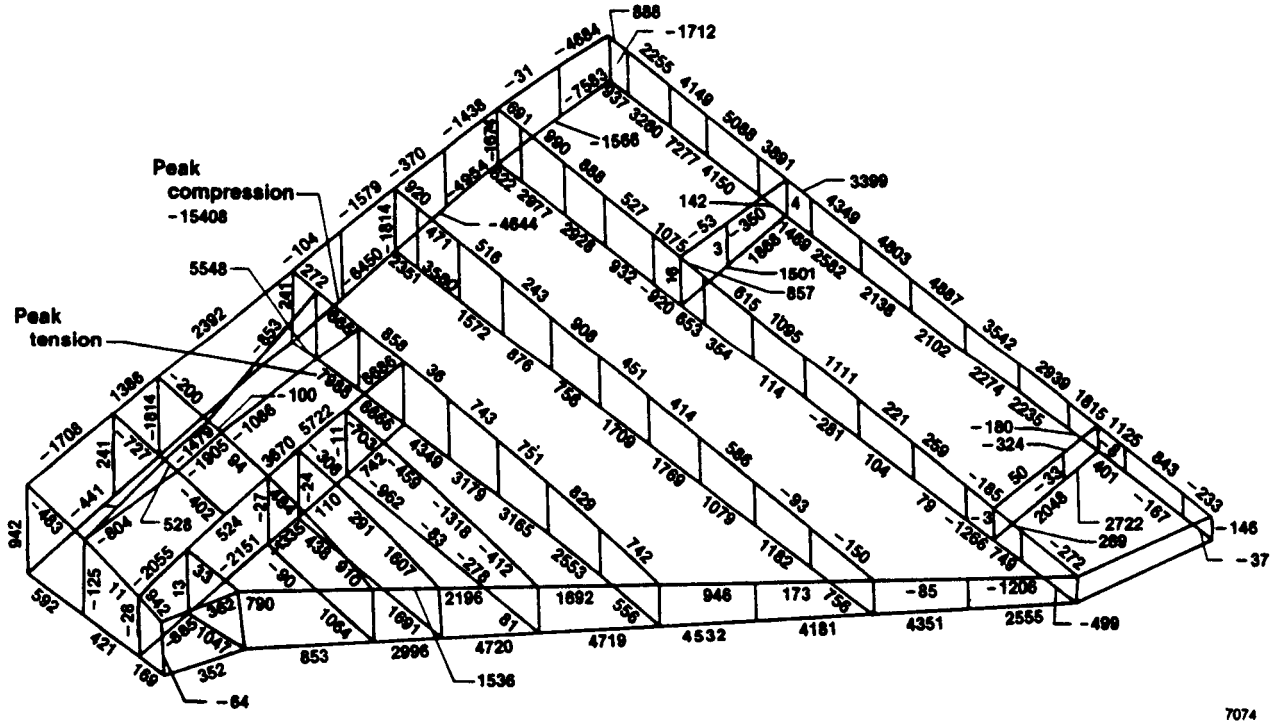

Figure 20. Axial stresses (in lb/in^2) in the orbiter wing spar caps, wing root rib caps, and other rod elements. STS-5 thermal loading. Time = 1700 sec.

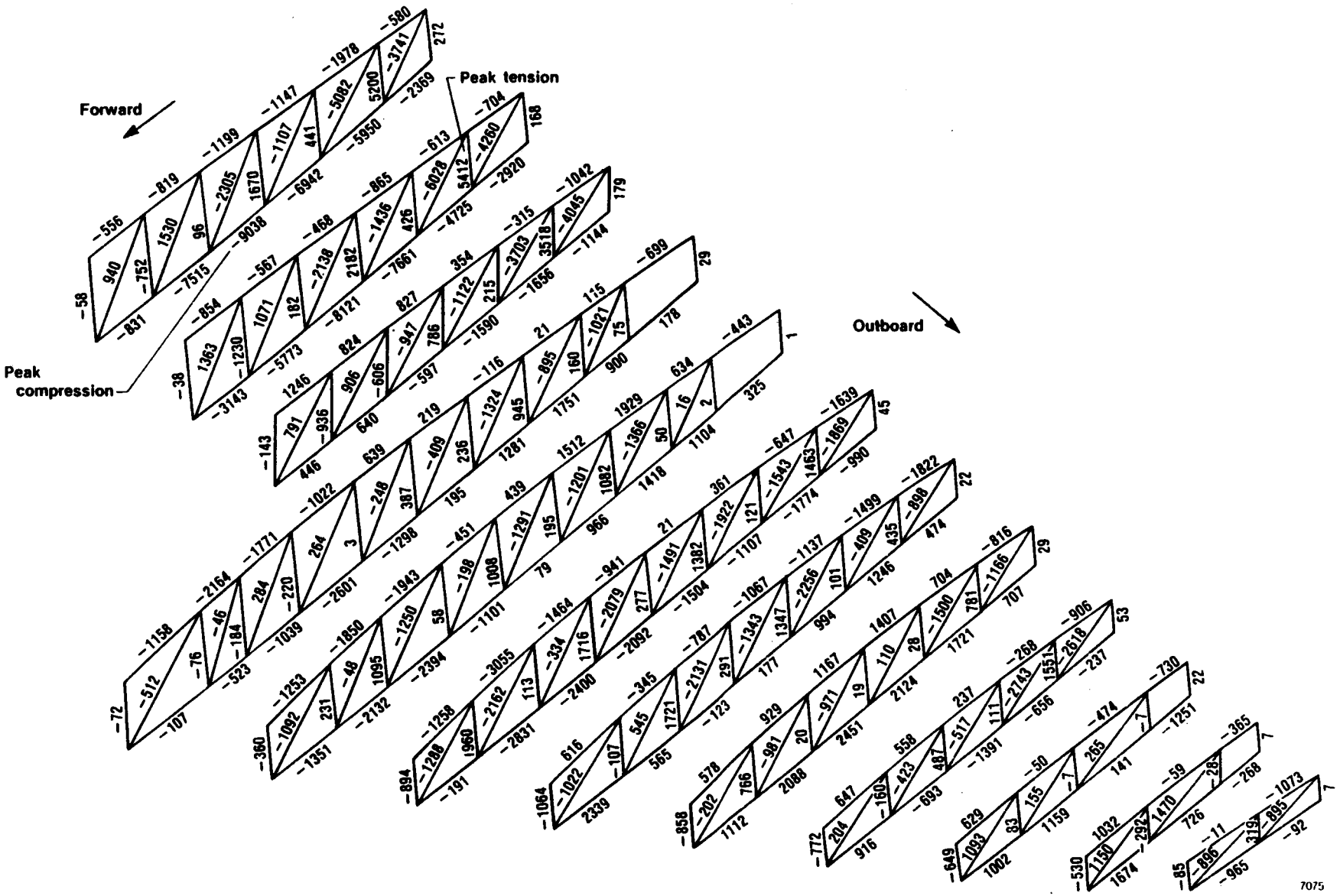

Figure 21. Axial stresses (in lb/in^2) in the orbiter wign rib truss members. STS-5 thermal loading. Time = 1700 sec.

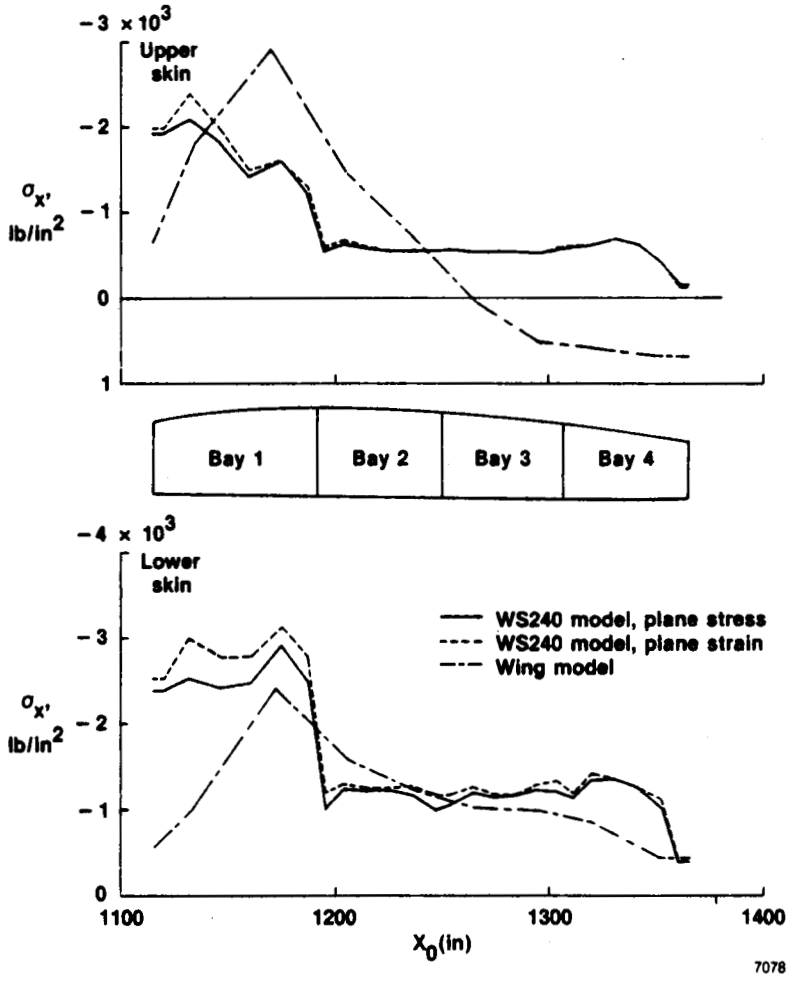

Figure 22. Chordwise distributions of normal stress σ_x in the orbiter wing skins at $|Y_0| \approx 240$, induced by STS-5 thermal loading. Time = 1700 sec.

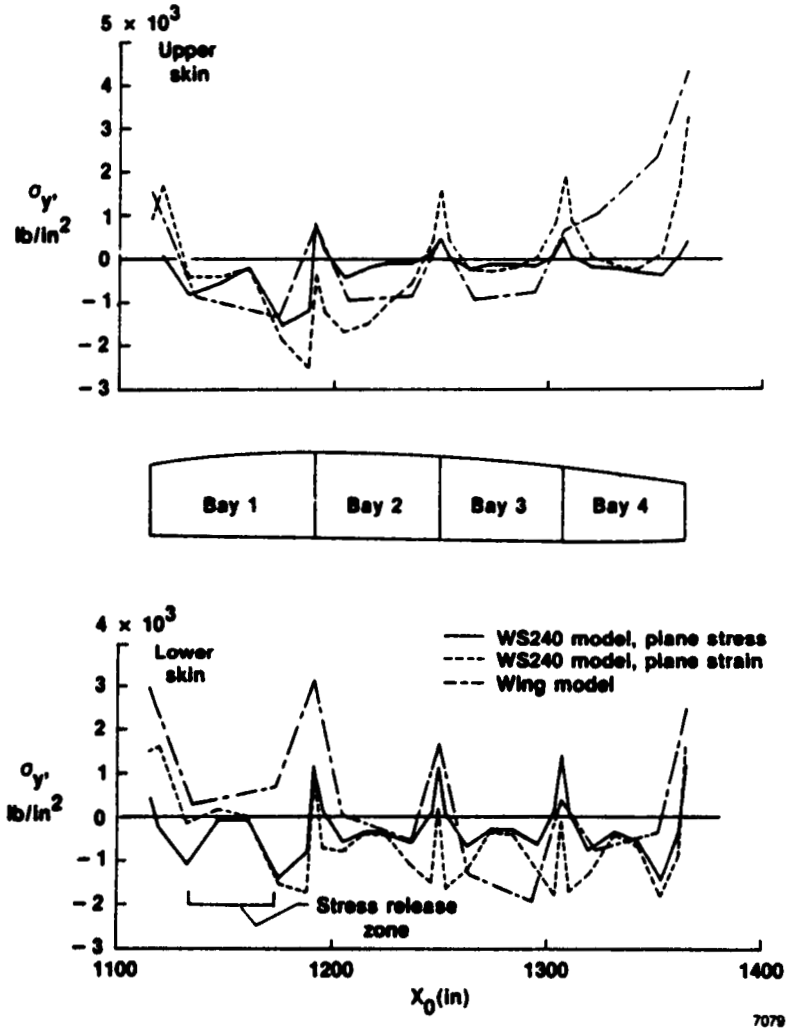

Figure 23. Chordwise distributions of normal stress σ_y in the orbiter wing skins at $|Y_0|$ 240, induced by STS-5 thermal loading. Time = 1700 sec.

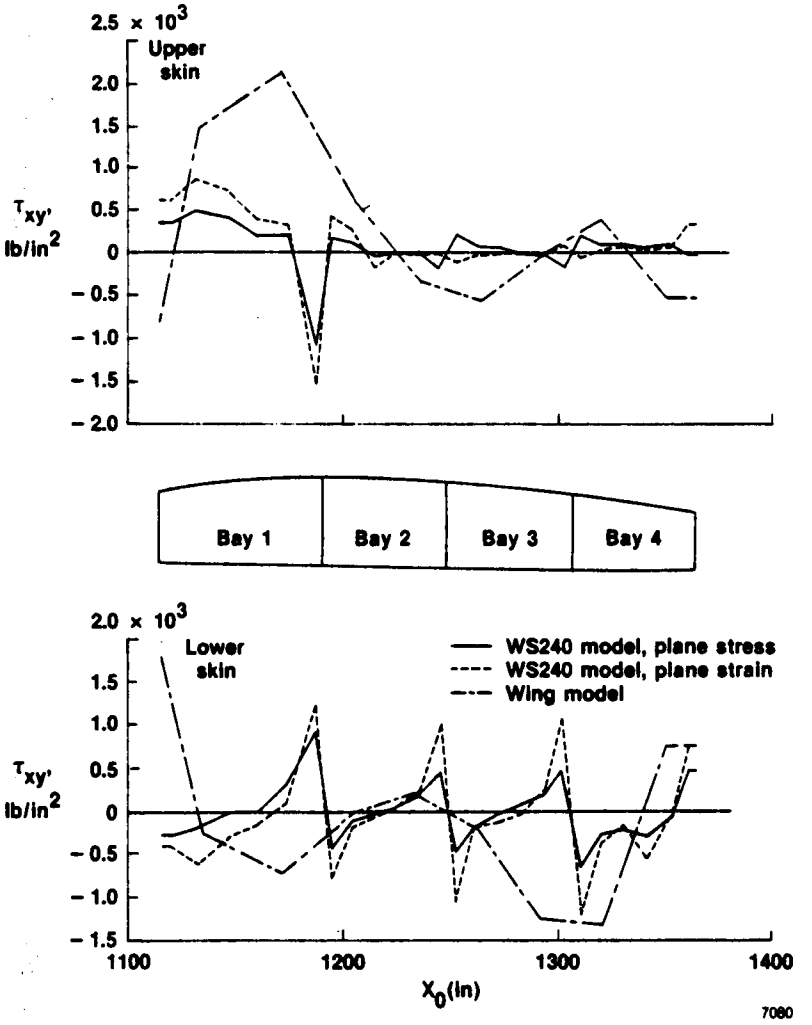

Figure 24. Chordwise distributions of shear stress τ_{xy} in the orbiter wing skins at Y_0-240, induced by STS-5 thermal loading. Time = 1700 sec.

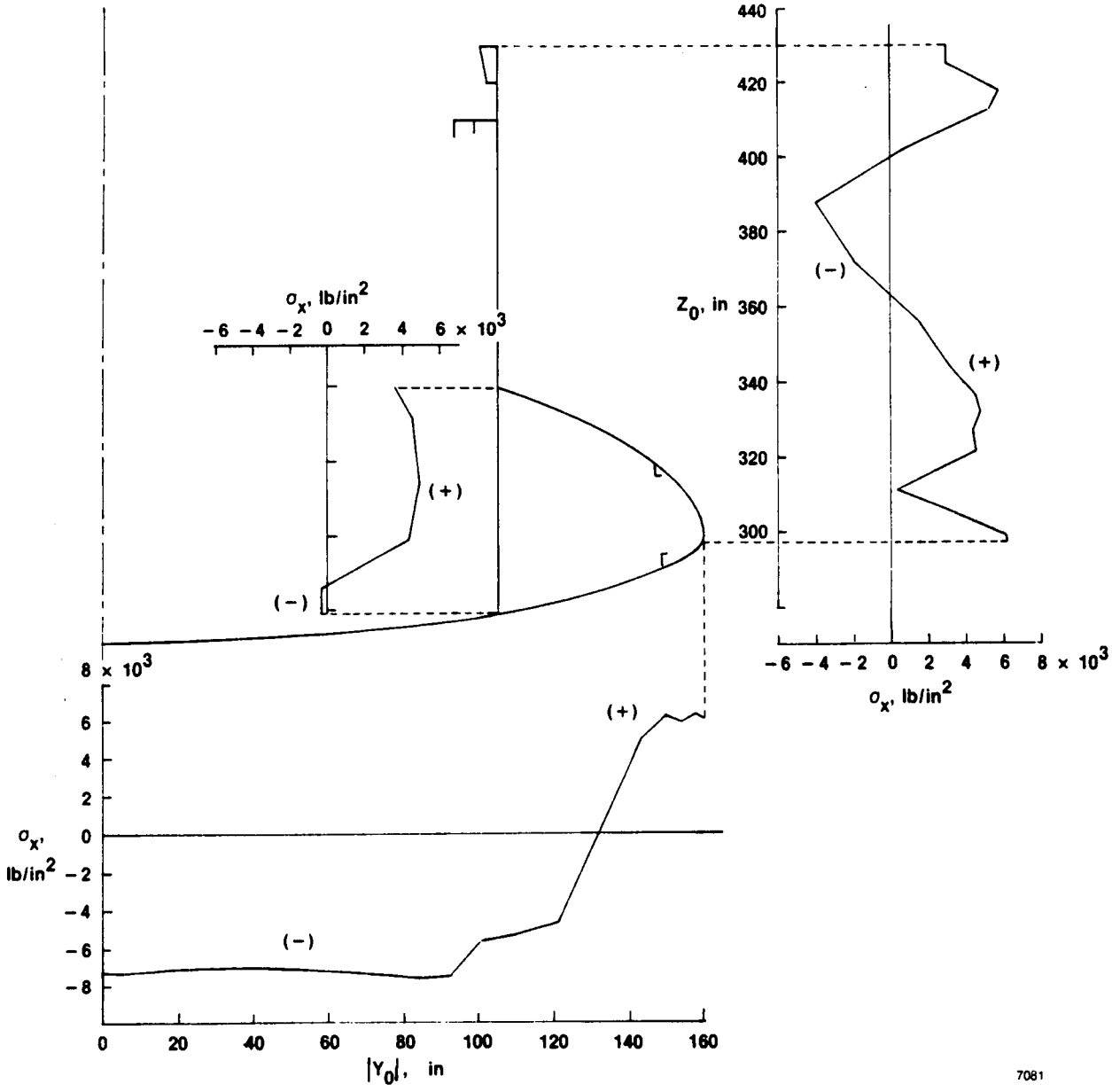

Figure 25. Distribution of axial stress σ_x in the orbiter fuselage at station $X_0$877. STS-5 thermal loading. Time = 1700 sec.

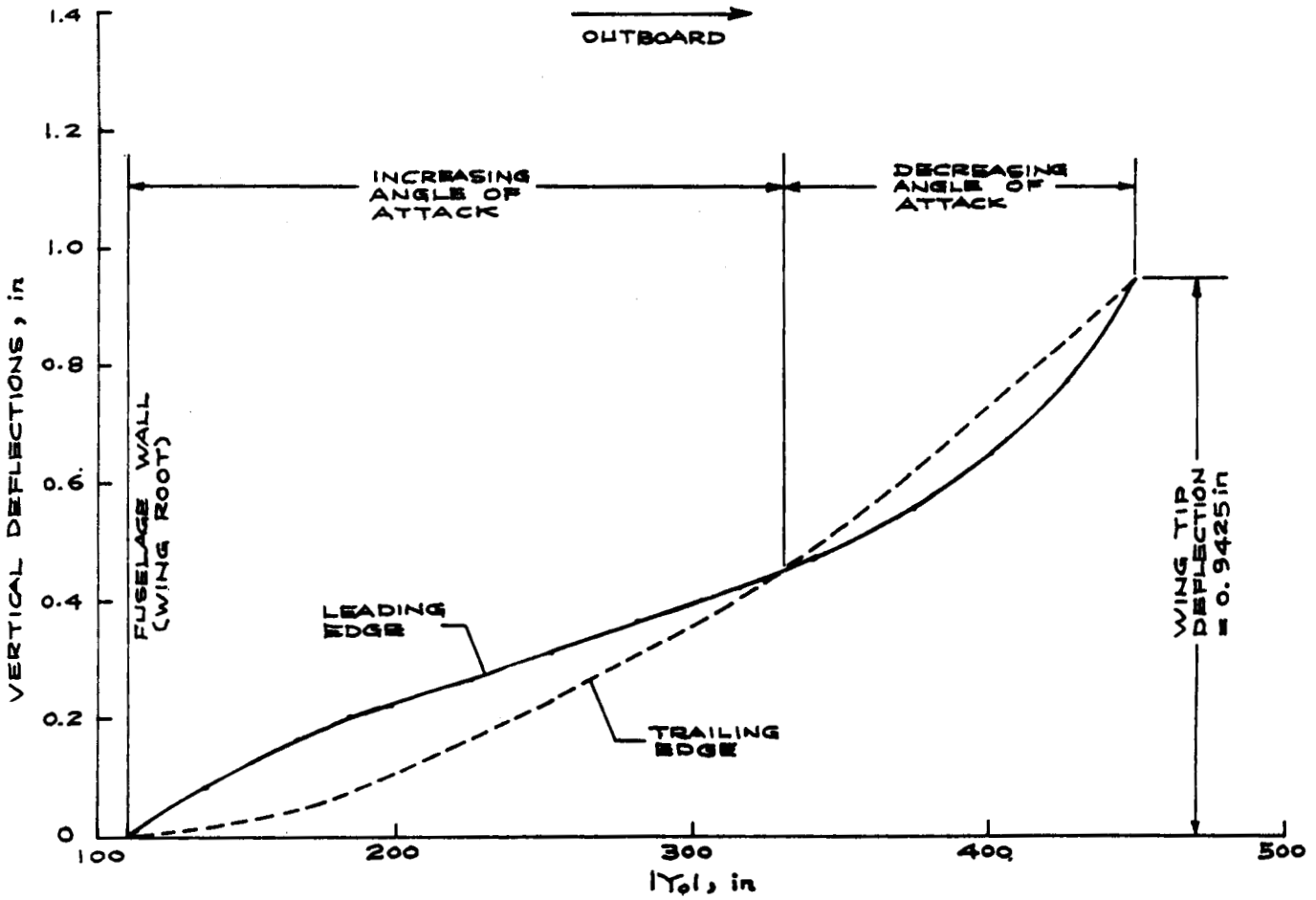

Figure 26. Deflection curves of leading and trailing edges of orbiter wing caused by STS-5 thermal loading. Time = 1700 sec. View looking aft.

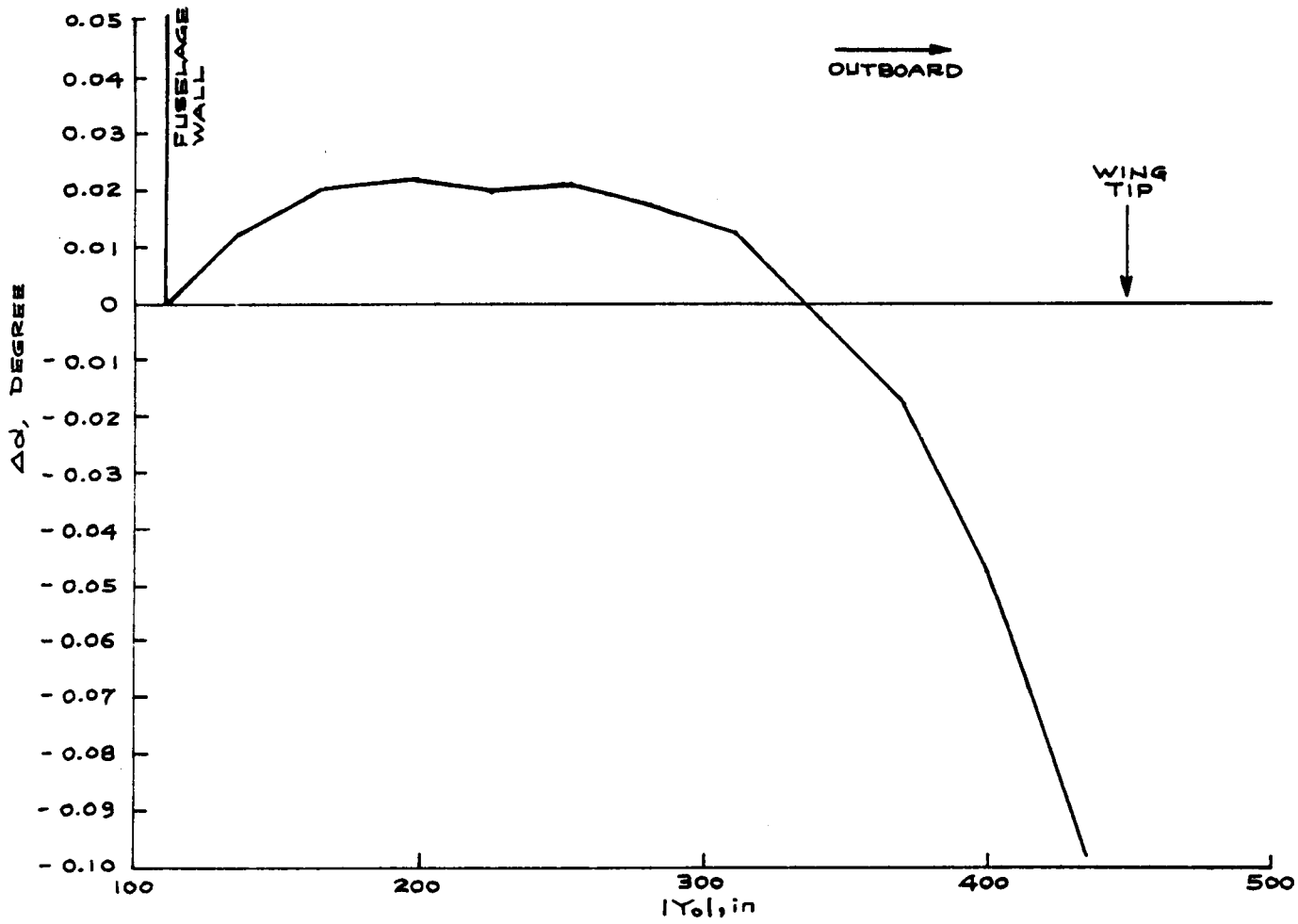

Figure 27. Spanwise change in angle of attack of orbiter wing caused by STS-5 thermal loading. Time = 1700 sec.

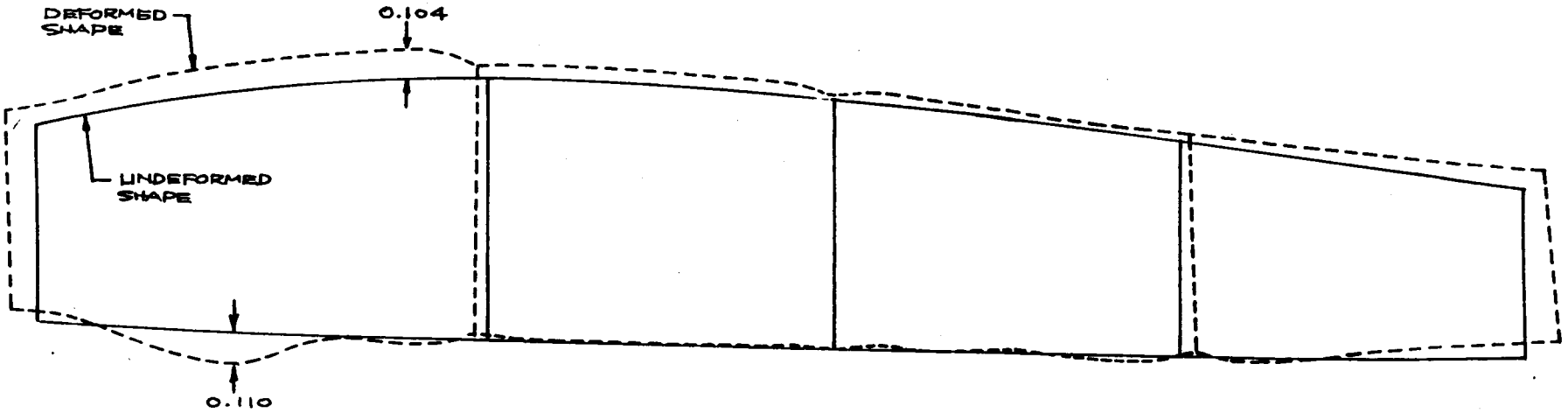

a. FREE EDGE/NO ROTATION

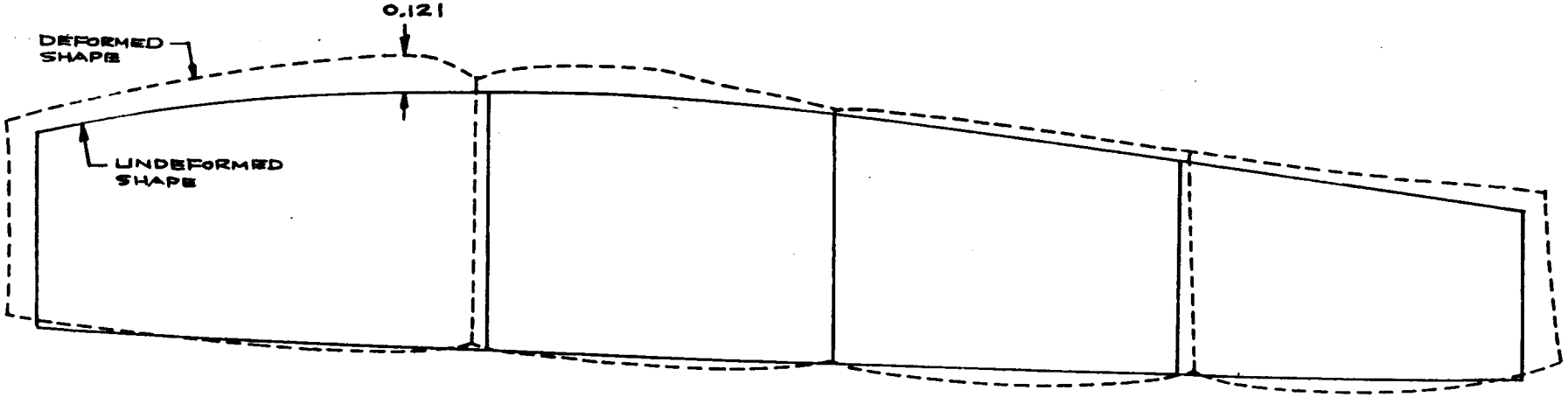

b PLANE STRAIN

Figure 28. Deformed shapes of wing cross section at $|Y_0|$ 240. STS-5 thermal loading. Time = 1700 sec. Dimensions are in inches.

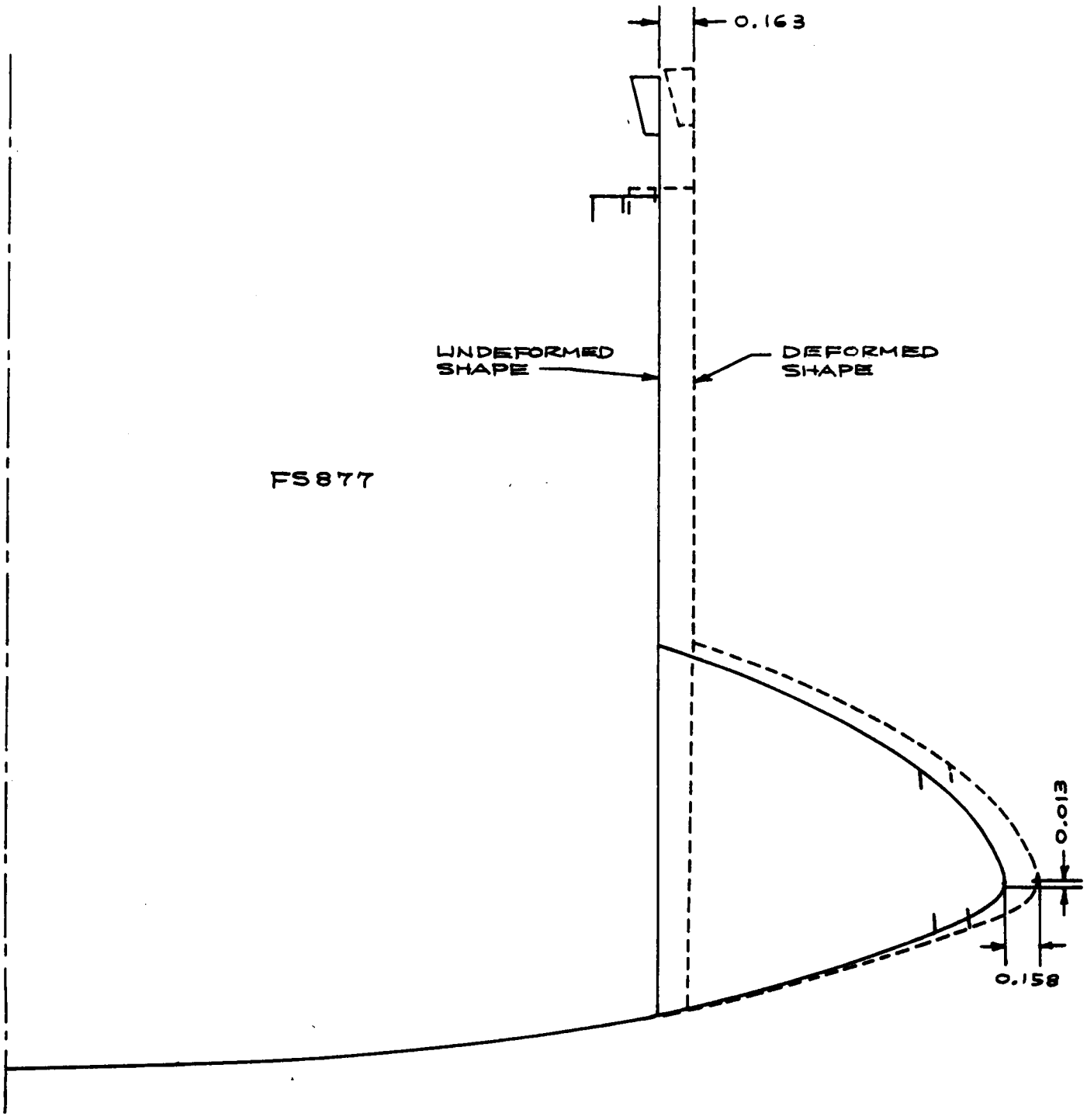

Figure 29. Deformed shape of fuselage cross section at $X_0$877. STS-5 thermal loading. Time = 1700 sec. Dimensions are in inches.

1. Report No. NASA TM-88286	2. Government Accession No.	3. Recipient's Catalog No.
4. Title and Subtitle THERMAL STRESS ANALYSIS OF SPACE SHUTTLE ORBITER SUBJECTED TO REENTRY AERODYNAMIC HEATING		5. Report Date October 1987 6. Performing Organization Code
7. Author(s) William L. Ko and Roger A. Fields		8. Performing Organization Report No. H-1400 10. Work Unit No. RTOP 505-53-51
9. Performing Organization Name and Address NASA Ames Research Center Dryden Flight Research Facility P.O. Box 273 Edwards, CA 93523-5000		11. Contract or Grant No. 13. Type of Report and Period Covered Technical Memorandum
12. Sponsoring Agency Name and Address National Aeronautics and Space Administration Washington, DC 20546		14. Sponsoring Agency Code
15. Supplementary Notes		

16. Abstract

A structural performance and resizing (SPAR) finite-element computer program and NASA structural analysis (NASTRAN) finite-element computer programs were used in the thermal stress analysis of the space shuttle orbiter subjected to reentry aerodynamic heating. A SPAR structural model was set up for the entire left wing of the orbiter, and NASTRAN structural models were set up for (1) a wing segment located at midspan of the orbiter left wing and (2) a fuselage segment located at midfuselage. The thermal stress distributions in the orbiter structure were obtained and the critical high thermal stress regions were identified. It was found that the thermal stresses induced in the orbiter structure during reentry were relatively low. The thermal stress predictions from the whole wing model were considered to be more accurate than those from the wing segment model because the former accounts for temperature and stress effects throughout the entire wing.

17. Key Words (Suggested by Author(s))	18. Distribution Statement		
Finite-element modelings Space shuttle orbiter STS-5 heating Thermal stress analysis	Unclassified — Unlimited Subject category 39		
19. Security Classif. (of this report) Unclassified	20. Security Classif. (of this page) Unclassified	21. No. of Pages 37	22. Price* A03

For sale by the National Technical Information Service, Springfield, Virginia 22161.